

Cell-type-specific profiling of brain mitochondria reveals functional and molecular diversity

Caroline Fecher^{1,2,3,18}, Laura Trovò^{1,2,18}, Stephan A. Müller^{1,2,4}, Nicolas Snaidero^{1,2}, Jennifer Wettmarshausen^{5,6}, Sylvia Heink^{1,7}, Oskar Ortiz^{8,9,15}, Ingrid Wagner¹⁰, Ralf Kühn^{1,8,9,16,17}, Jana Hartmann¹¹, Rosa Maria Karl¹¹, Arthur Konnerth^{11,12,13}, Thomas Korn^{1,7,12}, Wolfgang Wurst^{2,8,9,12}, Doron Merkler^{1,10,14}, Stefan F. Lichtenthaler^{2,4,12}, Fabiana Perocchi^{5,6,12} and Thomas Misgeld^{1,2,12,13*}

Mitochondria vary in morphology and function in different tissues; however, little is known about their molecular diversity among cell types. Here we engineered *MitoTag* mice, which express a Cre recombinase-dependent green fluorescent protein targeted to the outer mitochondrial membrane, and developed an isolation approach to profile tagged mitochondria from defined cell types. We determined the mitochondrial proteome of the three major cerebellar cell types (Purkinje cells, granule cells and astrocytes) and identified hundreds of mitochondrial proteins that are differentially regulated. Thus, we provide markers of cell-type-specific mitochondria for the healthy and diseased mouse and human central nervous systems, including in amyotrophic lateral sclerosis and Alzheimer's disease. Based on proteomic predictions, we demonstrate that astrocytic mitochondria metabolize long-chain fatty acids more efficiently than neuronal mitochondria. We also characterize cell-type differences in mitochondrial calcium buffering via the mitochondrial calcium uniporter (Mcu) and identify regulator of microtubule dynamics protein 3 (Rmdn3) as a determinant of endoplasmic reticulum-mitochondria proximity in Purkinje cells. Our approach enables exploring mitochondrial diversity in many *in vivo* contexts.

Mitochondria perform different tasks in diverse cell types. For instance, mitochondria control differentiation of immune and stem cells^{1,2}. Similarly, in the nervous system, mitochondria regulate neurite branching and regeneration³, as well as synaptic strength, stability and signaling⁴. Although some of these cell-type-specific functions are achieved by modulating the well-characterized metabolic roles of mitochondria, less-expected functions emerge, for example, in immune or redox signaling^{5,6}, and likely many more remain elusive.

Bulk mitochondrial proteomes vary between tissues⁷. Nevertheless, it remains unclear to what degree such diversity reflects tissue-specific global differences or variations in cellular composition. Moreover, genes that encode mitochondrial proteins are differentially expressed among tissues, cell types and even cell compartments⁸, but how much such transcriptional diversity results in mitochondrial proteome variability has not been resolved. Indeed, although the extrapolation of proteomics data from transcriptomes is generally problematic⁹, the mitochondrial proteome is uniquely complex, especially in cells of extended geometry, such as neurons³. Hence in these complex cell types it is crucial to directly measure proteomic variability. Moreover, it is important to obtain functional mitochondria from the respective cell of interest to test any resulting predictions.

Here, we describe an approach that allows isolation of functional mitochondria from essentially any cell type. This approach is based

on a *MitoTag* mouse, which faithfully expresses an outer mitochondrial membrane (OMM)-targeted green fluorescent protein (GFP) in a Cre recombinase (Cre)-dependent manner. This innocuous and efficient epitope allows capturing of cell-type-specific mitochondria. We highlight the power of our approach by comparing neural mitochondria of the three major cell populations from the cerebellum. Thus, we (1) provide a systematic profiling of cell-type-specific variability among mitochondrial proteomes *in situ* and (2) identify numerous cell-type-specific mitochondrial markers that are suitable to characterize cell-type-specific mitochondria in the healthy and diseased mouse and human brain. On this basis, we predict and prove differences between mitochondria from different cerebellar cell types regarding (3) beta-oxidation, (4) calcium buffering via the mitochondrial calcium uniporter (Mcu) and (5) organelle contacts mediated by the tether regulator of microtubule dynamics protein 3 (Rmdn3).

Results

***MitoTag* mice innocuously tag cell-type-specific mitochondria *in vivo*.** Previous work established tagging of macromolecular structures such as ribosomes to explore cell-type-specific mRNA translation profiles *in situ*¹⁰. This approach recently has been extended to organelles, for example, to explore mitochondrial¹¹ and lysosomal¹² metabolomes *in vitro* or organellar DNA in invertebrates¹³,

¹Institute of Neuronal Cell Biology, Technical University of Munich, Munich, Germany. ²German Center for Neurodegenerative Diseases, Munich, Germany. ³Graduate School of Systemic Neurosciences, Ludwig-Maximilians University, Munich, Germany. ⁴Neuroproteomics, School of Medicine, Klinikum rechts der Isar and Institute for Advanced Study, Technical University of Munich, Munich, Germany. ⁵Gene Center Munich, Ludwig-Maximilians University, Munich, Germany. ⁶Institute for Diabetes and Obesity, Helmholtz Zentrum München, Munich, Germany. ⁷Experimental Neuroimmunology, Klinikum rechts der Isar, Technical University of Munich, Munich, Germany. ⁸Institute of Developmental Genetics, Helmholtz Zentrum München, Munich, Germany. ⁹Institute of Developmental Genetics, Technical University of Munich, Munich, Germany. ¹⁰Department of Pathology and Immunology, University of Geneva, Geneva, Switzerland. ¹¹Institute of Neuroscience, Technical University of Munich, Munich, Germany. ¹²Munich Cluster for Systems Neurology, Munich, Germany. ¹³Center of Integrated Protein Science, Munich, Germany. ¹⁴Division of Clinical Pathology, Geneva University Hospital, Geneva, Switzerland. ¹⁵Present address: Merck KGaA, Darmstadt, Germany. ¹⁶Present address: Max-Delbrück-Centrum für Molekulare Medizin, Berlin, Germany. ¹⁷Present address: Berlin Institute of Health, Berlin, Germany. ¹⁸These authors contributed equally: Caroline Fecher, Laura Trovò. *e-mail: thomas.misgeld@tum.de

or to correlate transcriptional and epigenetic signatures¹⁴. To study mitochondrial diversity among cell types in situ using mitochondria that are directly derived from their tissue context, we generated a reporter line, named *MitoTag* mouse (Fig. 1a). *MitoTag* mice harbor in their *Rosa26* locus a floxed 'stop' expression cassette, which drives expression of GFP targeted to the OMM in a Cre-dependent manner (GFP-OMM). To achieve GFP-OMM expression in diverse cell types of the CNS, we crossed *MitoTag* mice to different Cre-driver lines (Supplementary Fig. 1) or neonatally injected them with adeno-associated virus to deliver Cre in a cell-type-specific manner (Supplementary Fig. 1f). Initial characterization was performed on: (1) Emx1:Cre crossed to *MitoTag* mice (abbreviated as Emx1:Cre/GFP-OMM), where the great majority of forebrain neurons and glia contained GFP-OMM-tagged mitochondria (Fig. 1b and Supplementary Fig. 1a); and (2) ChAT:Cre/GFP-OMM mice, where mitochondria in cholinergic neurons, including motor neurons, are tagged (ChAT, choline acetyltransferase; Supplementary Fig. 1b). First, we confirmed mitochondrial localization of GFP-OMM by counterstaining Emx1:Cre/GFP-OMM cortex with the endogenous inner mitochondrial membrane protein cytochrome c oxidase subunit 4 isoform 1 (Cox4i1; Fig. 1c). We corroborated OMM localization by expansion microscopy in Emx1:Cre/GFP-OMMxThy1:mito-RFP mice (Fig. 1d), which additionally express matrix-localized red fluorescent protein (mito-RFP) in neurons. Second, we used ChAT:Cre/GFP-OMM mice to rule out adverse transgene effects on mitochondrial and cellular health in motor neurons by measuring mitochondrial transport and shape, as well as neuromuscular synapse morphology (Supplementary Fig. 2a–d). Finally, the crude mitochondrial fraction (CMF) from Emx1:Cre/GFP-OMM cortex showed unchanged oxygen consumption rates (OCRs) compared with controls (Supplementary Fig. 2e).

To isolate GFP-OMM-tagged mitochondria, we optimized an immunocapture protocol using anti-GFP magnetic microbeads (IC GFP; Fig. 1e). This method is well established for mitochondria based on anti-Tom22 microbeads¹⁵ but recently has been expanded to neoantigens^{11,13}. Indeed, for Emx1:Cre/GFP-OMM cortex, western blot analysis corroborated efficient mitochondrial enrichment via IC GFP (Supplementary Fig. 3a). Using electron microscopy, we found that the majority of GFP-captured objects were isolated mitochondria with well-preserved ultrastructure, in contrast with the CMF, which contained synaptosome-enclosed mitochondria and myelin debris (Fig. 1f). Moreover, mitochondria that were immunocaptured from either control cortex (Cre⁻ *MitoTag* mice; IC Tom using anti-Tom22 microbeads) or Emx1:Cre/GFP-OMM cortex (~74% GFP-OMM-tagged mitochondria; Supplementary Fig. 4b) did not differ in respiratory capacity (Fig. 1g).

***MitoTag* mice allow isolation of cell-type-specific mitochondria from complex tissues in situ.** A major concern in enriching cell-type-specific mitochondria from tissue is that during the isolation, mitochondria from different cells could merge by clumping or fusion¹⁶. Indeed, we observed that once we pelleted mitochondria by centrifugation, separation via IC GFP was impaired. Therefore, to determine the selectivity of our immunocapture, we devised 'spike-in' experiments with mitochondria carrying mito-RFP. First, we used an ex vivo mixing experiment where cortices from Emx1:Cre/GFP-OMM mice and Thy1:mito-RFP mice were mixed one to one (50:50%) and subjected to immunocapture (Fig. 2a(i)). Using western blot analysis, we observed that IC Tom recovered the initial GFP-OMM/mito-RFP ratio of the CMF, whereas tagged mitochondria were selectively enriched with IC GFP (GFP-OMM: 4.7-fold compared with IC Tom; Fig. 2b,c and Supplementary Fig. 5a). We mimicked cell populations with various abundance by mixing the postnuclear fractions from Emx1:Cre/GFP-OMM and Thy1:mito-RFP cortex in different ratios, and found that the isolation efficacy stayed stable down to dilutions of 1:20 (Supplementary

Fig. 5b,c). Throughout, we detected ~5% of mito-RFP in IC GFP. To corroborate this experiment in vivo, we used ChAT:Cre/GFP-OMM cortex, where less than 1% of mitochondria are tagged (Supplementary Fig. 4b), representing a low abundant population of exclusively axonal mitochondria from cholinergic neurons. Still, the immunocapture allowed us to enrich substantial amounts of mitochondria (Supplementary Fig. 5d). Finally, to corroborate enrichment of tagged mitochondria from tissue, we immunocaptured astrocytic mitochondria from Gfap:Cre/GFP-OMMxThy1:mito-RFP cortex (Fig. 2a(ii)). This tissue contained ~29% GFP-OMM-labeled mitochondria from astrocytes and 63% mito-RFP-positive neuronal mitochondria (Supplementary Fig. 4b). Here, GFP-OMM was enriched by 7.4-fold compared with IC Tom from immediately adjacent cells (Fig. 2d).

Label-free proteomics demonstrates mitochondrial diversity in the adult cerebellum. The cerebellum is composed of various well-characterized cell types, for which specific Cre-driver lines are available, and it is prone to mitochondrial dysfunction. Thus, we used the cerebellum as a proof-of-concept to test whether our *MitoTag* approach could resolve cellular diversity of the mitochondrial proteome in situ. First, we generated *MitoTag* lines for the following cell types (Fig. 3a and Supplementary Fig. 1c–e): (1) Purkinje cells (PC), the major inhibitory neuron of the cerebellum, via L7:Cre; (2) granule cells (GC), the most abundant excitatory neuron, via Gabra6:Cre; and (3) astrocytes (A) via Gfap:Cre. Next, we developed a label-free proteomic workflow for the comparison of mitochondrial proteomes that involved immunocapture of cell-type-specific mitochondria (IC GFP) and total tissue mitochondria (IC Tom) per biological replicate ($n \geq 5$ mice; Supplementary Fig. 6). IC Tom provided an 'average mitochondrial proteome' from the cerebellum, thereby correcting for variation among experiments and mouse cohorts. In this background proteome, we quantified 3,718 proteins, which we compared with reference proteomics datasets from mouse cerebellar mitochondria⁷ and from whole cerebellum¹⁷, revealing a coverage of 68% *MitoCarta*¹⁸ annotated proteins (Supplementary Fig. 3b). Moreover, intensity-based absolute quantification (iBAQ) demonstrated strong enrichment of mitochondrial proteins over nonmitochondrial proteins (for example, 6.51-fold for immunocaptures from cerebellum; Supplementary Fig. 3c), despite our deliberate choice of a 'conservative' isolation approach with the aim to include transiently OMM-associated proteins for discovery and preserve organelle functionality (see Methods). In comparison, our proteome obtained from whole cerebellum revealed that mitochondrial proteins were 2.64-fold more abundant than nonmitochondrial proteins. In contrast, a published proteome of cerebellar mitochondria purified by Percoll⁷ uncovered a 6.57-fold increased abundance of mitochondrial over nonmitochondrial proteins, matching our own enrichment with immunocapture. Indeed, 56.5% of peptides accounted for mitochondrial proteins in immunocaptures (Supplementary Fig. 3d). Importantly, mitochondrial proteins showed more prominent abundance changes than nonmitochondrial proteins. For example, 23.1% of mitochondrial annotated proteins from PC showed a significant abundance change (IC GFP/IC Tom ratio >1.5 or <0.67 ; $P < 0.05$), whereas only 4.0% of nonmitochondrial proteins were significantly changed, suggesting that most of the latter are not specifically captured.

In total, >85% of identified proteins were shared among all three cell types (Supplementary Fig. 6). We identified 196 candidates with differential expression (\log_2 fold change (FC) $\geq |1|$ between cell types), of which 89.8% are mitochondrial annotated. Of these, 18, 51 and 114 were exclusively enriched in one cell type (Fig. 3b and Supplementary Fig. 7d). An additional 13 proteins showed shared enrichment in two cell types. When we compared proteins from astrocytic mitochondria against either mitochondria from GC (y axis; Fig. 3c and Supplementary Fig. 7a) or PC (x axis; Fig. 3c and

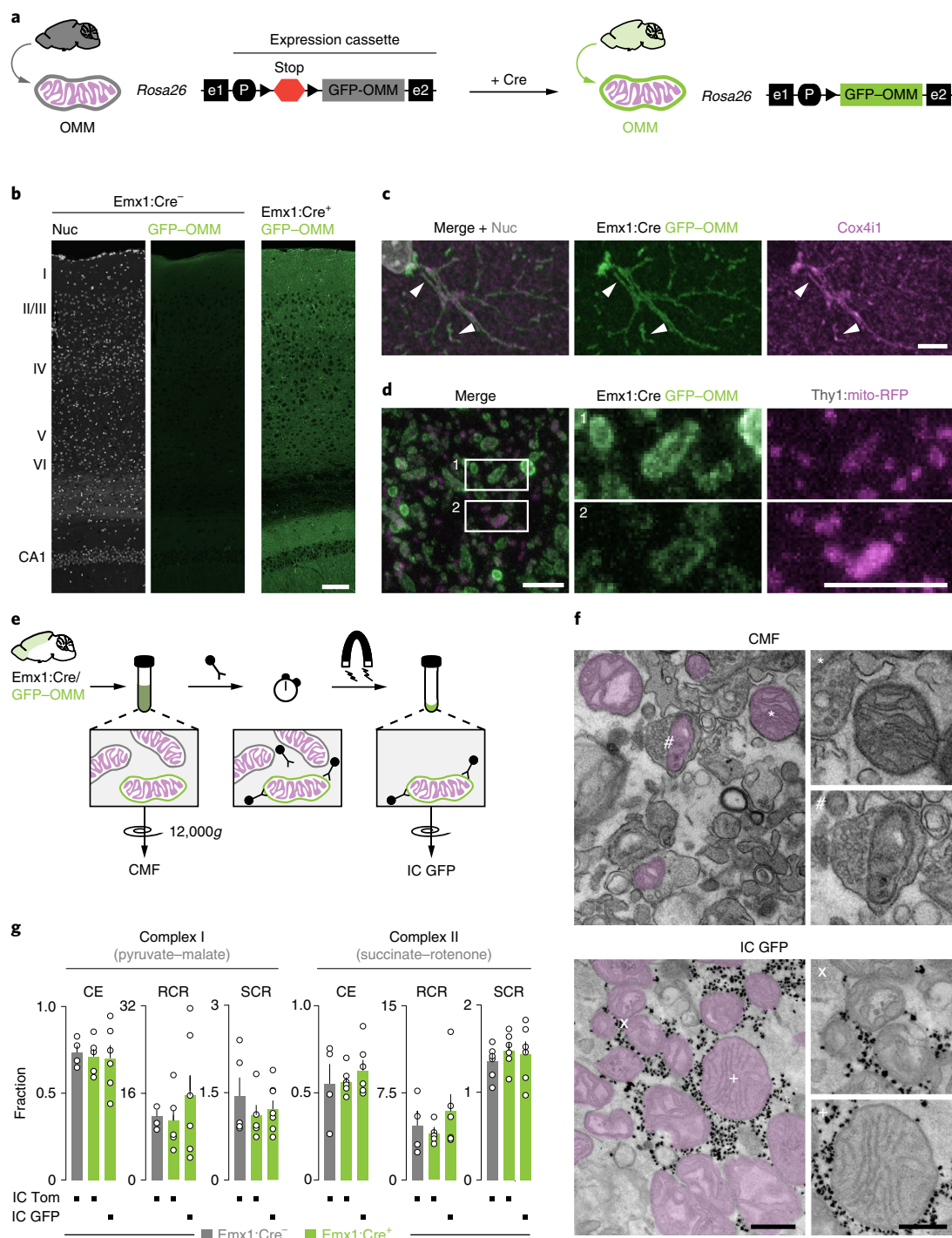


Fig. 1 | MitoTag mice allow isolation of intact and functional mitochondria from cells in situ. **a**, GFP-OMM insertion into the mouse *Rosa26* locus. **b**, Absence of expression in stopped *MitoTag* cortex (left and middle; *Cre^{-/-}*), but GFP-OMM (green) in neural cells from *Emx1:Cre/GFP-OMM* mice (right; *Cre^{+/+}*). Nuclear counterstain (Nuc; white) is shown in the left panel. **c**, Immunostaining of the *Emx1:Cre/GFP-OMM* cerebral cortex for Cox4i1 (magenta) confirms mitochondrial localization of GFP-OMM (arrowheads). **d**, Expansion microscopy of *Emx1:Cre/GFP-OMM* Thy1:mito-RFP cerebral cortex shows localization of GFP-OMM in the OMM (green) surrounding mito-RFP (magenta), which is localized to the mitochondrial matrix of a large subset of neurons. **e**, Immunocapture of GFP-OMM-tagged mitochondria (IC GFP). **f**, Electron micrographs comparing the CMF from *Emx1:Cre/GFP-OMM* cortex with IC GFP. Note the free mitochondria (*) and synaptosome-enclosed mitochondria (#) found in CMF (top) and free, intact mitochondria (X, +) with microbeads (black dots in micrograph; bottom). **g**, Bioenergetic parameters derived from oxygen consumption measurements in the presence of pyruvate-malate (left) and succinate-rottenone (right) as substrates for immunocaptured mitochondria. Mitochondria were immunocaptured from *Emx1:Cre^{-/-}*/GFP-OMM or *Emx1:Cre^{+/+}*/GFP-OMM cortex using Tom22 (pan-mitochondrial, IC Tom) or GFP-OMM (cell-type-specific mitochondria, IC GFP) as bait (no significant differences observed with one-way ANOVA with post hoc testing; $n \geq 4$ mice from at least three independent experiments). Dot plot: mean \pm s.e.m. Images show representative results from $n = 5$ (**b,c**) and $n = 2$ (**d,f**) independent experiments. Scale bars: 100 μ m (**b**); 500 nm (**d,f**) (250 nm in insets). CE, coupling efficiency; CMF, crude mitochondrial fraction; e1/2, exon 1/2; Nuc, nuclear counterstain; P, promoter; RCR, respiratory capacity ratio; SCR, spare capacity ratio.

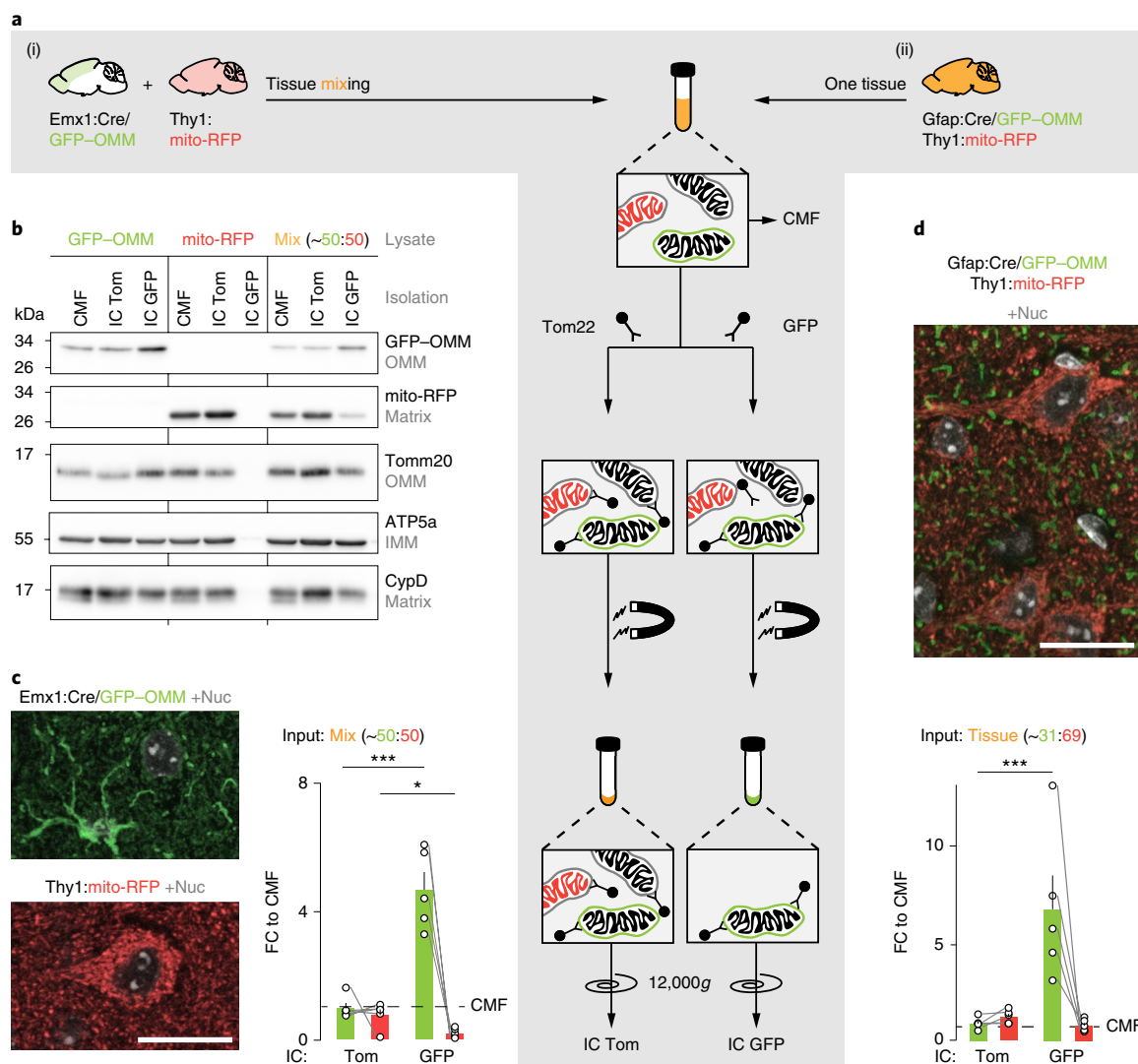


Fig. 2 | Immunocapture from MitoTag mice enriches cell-type-specific mitochondria without mitochondrial cross-contamination from other cells.

a, ‘Spike-in’ experiments to demonstrate enrichment of GFP-OMM-tagged mitochondria from other mitochondria (mito-RFP). Using the cortex, we mixed two mitochondrial populations (GFP-OMM and mito-RFP) either ex vivo on the tissue level (i) or in vivo (ii) by breeding *Gfap:Cre/GFP-OMM* × *Thy1:mito-RFP* mice. **b,c**, Enrichment of GFP-OMM-labeled mitochondria after immunocapture via GFP-OMM (IC GFP), but not via Tom22 (IC Tom), from the ex vivo mixing experiment (schematic in **a**(i)). The cortices from *Emx1:Cre/GFP-OMM* (**c**, top micrograph for tissue expression; GFP-OMM, green; Nuc, white) and from *Thy1:mito-RFP* (**c**, bottom micrograph; mito-RFP, red) were mixed in a 50:50 ratio before lysate generation (**b**; mix, orange). **b**, Western blot probing for GFP-OMM, mito-RFP and mitochondrial proteins (Tom22, OMM; ATP5a, inner mitochondrial membrane (IMM); CypD, matrix). Note enrichment of GFP-OMM via IC GFP from pure *Emx1:Cre/GFP-OMM* tissue (lysate: GFP-OMM) and the absence of any mitochondrial isolation from pure mito-RFP tissue (lysate: mito-RFP). Representative results from $n = 2$ independent experiments. Mixing condition is quantified in **c**. **c**, Quantification of ex vivo mixing experiment (**a**(i)) comparing isolations with initial CMF (GFP-OMM, green bar; $P = 0.0002$; mito-RFP, red bar; $P = 0.037$, one-tailed ratio-paired t -test; $n = 5$ isolations). Densitometry is normalized to mitochondrial content. Dot plot: mean \pm s.e.m. **d**, In vivo ‘spike-in’ experiment (**a**(ii)) using cortex from *Gfap:Cre/GFP-OMM* × *Thy1:mito-RFP* mice (micrograph for tissue expression) as starting material with an -31:69 ratio (ratio of GFP-OMM to mito-RFP mitochondria excluding nonlabeled organelles; see Supplementary Fig. 4b). Graph shows quantification from western blot analysis comparing isolations with initial CMF (GFP-OMM, $P = 0.0002$, one-tailed ratio-paired t -test; $n = 5$ isolations). Dot plot: mean \pm s.e.m. Scale bars: 20 μ m (**c,d**). CMF, crude mitochondrial fraction; FC, fold change; IC, immunocapture; Nuc, nuclear counterstain.

Supplementary Fig. 7b), we detected a separation in protein composition of neuronal mitochondria from glial mitochondria. Equally, the KEGG pathway and GO term process analysis (Supplementary Fig. 7e,f) confirmed differential specializations of neuronal (for example, ubiquinone biosynthesis) versus astrocytic mitochondria (for example, lipid metabolism). In contrast, other mitochondrial protein pathways, namely respiratory chain components, protein import and translation, tricarboxylic acid cycle showed no systematic differences, pointing to a conserved core of the mitochondrial proteome (Supplementary Fig. 8).

Cell-type-specific mitochondrial markers confirm mitochondrial diversity. We selected 28 proteins that our proteomics data predicted as cell type enriched for further validation based on literature and antibody availability, in addition to Cox4i1 as a ubiquitous mitochondrial marker and syntaphilin (Snph) as a known¹⁹ neuronal marker (which was not significantly enriched in the profiled cell types). Using immunofluorescence staining, we confirmed in all testable cases (21/28) our predicted cell-type-enriched expression and subcellular localization in mitochondria (Fig. 3d–f and Supplementary Fig. 9). Furthermore, we confirmed the specific fold

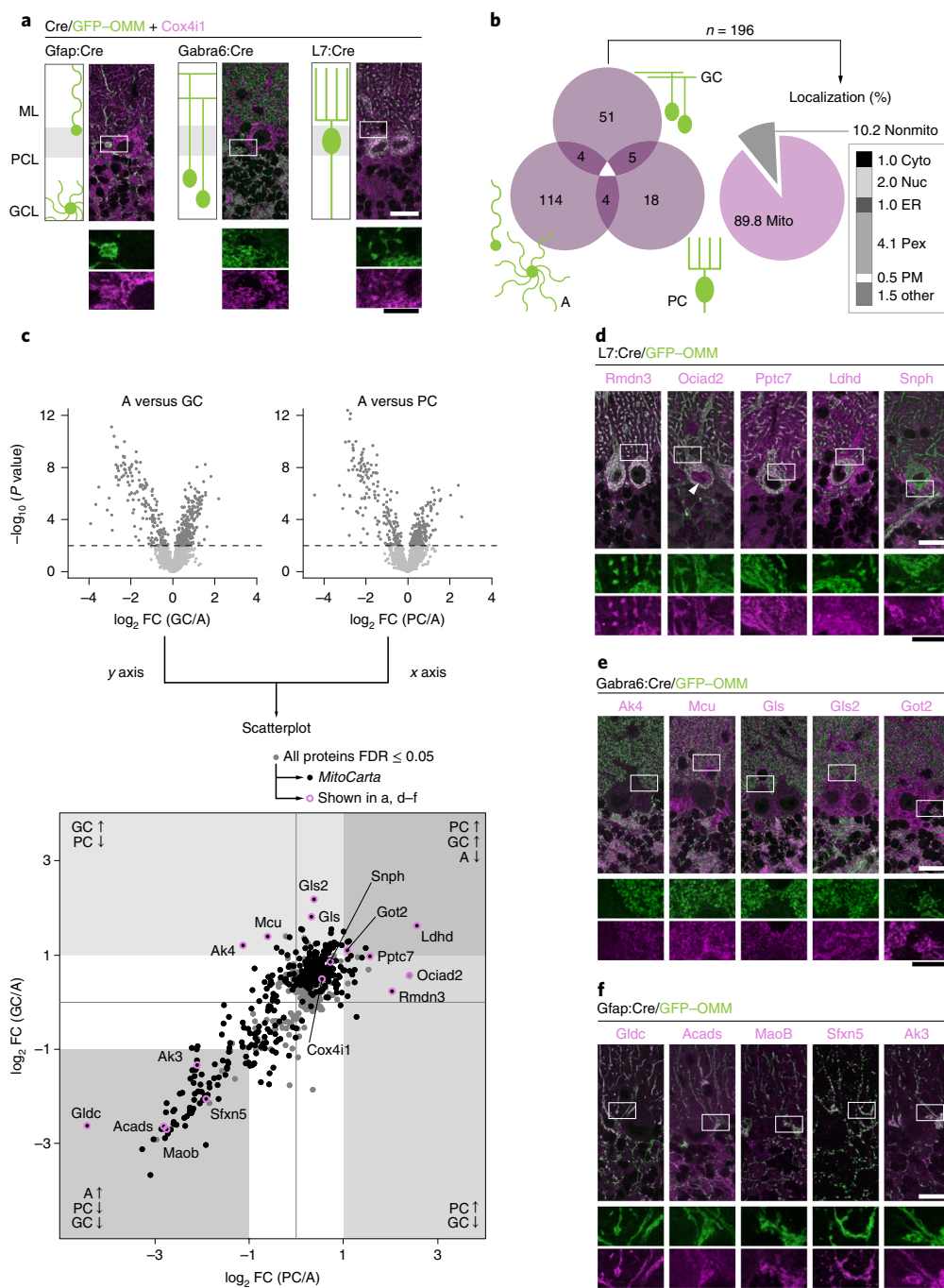


Fig. 3 | Proteomic profiling of cell-type-specific mitochondria in the adult mouse cerebellum. **a**, GFP-OMM expression patterns (green) and Cox4i1 staining (pan-mitochondrial; magenta) in the investigated cerebellar cell types: astrocytes-Bergmann glia (left; Gfap:Cre), excitatory GC (middle; Gabra6:Cre) and inhibitory PC (right; L7:Cre). Schematics show cell morphology and anatomic position within the cerebellum. Details show partial colocalization of cell-type-specific GFP-OMM with Cox4i1. **b**, Venn diagram depicting candidates ($n=196$) with cell-type-specific enrichment obtained by proteomics ($FC \geq |1|$) from the pairwise comparison between cell types) and their subcellular localization (Cyto, cytoplasmic; ER, endoplasmic reticulum; Mito, mitochondrial; Nonmito, nonmitochondrial; Nuc, nuclear; Pex, peroxisomal; PM, plasma membrane; and other). **c**, Comparison of cell-type-specific mitochondrial proteomes between cell types (top: volcano plots comparing GC/A (left) and PC/A (right); two-tailed t -test, $FDR \leq 0.05$, 500 randomizations, $n \geq 3$ quantifications) and among cell types (bottom: scatterplot of proteins merging the previous comparison between cell types ($FDR \leq 0.05$ in at least one comparison); x axis, PC/A; y axis, GC/A). In volcano plots, dark gray circles represent proteins with $FDR \leq 0.05$. In the scatterplot, all circles represent proteins from volcano plots with $FDR \leq 0.05$; black circles, *MitoCarta* annotated proteins; open magenta circles, candidates shown in **a** and **d-f**. FC, fold change. **d-f**, Validation of candidates by immunofluorescence staining in cerebellum. Candidates show prominent colocalization with cell-type-specific GFP-OMM (green), confirming the proteomics data (see **c**) of PC (**d**), GC (**e**) and astrocytes (**f**). Note the pan-neuronal patterns of Ldhd, Gls2 and Got2 (**d,e**) and the pinceau-like organization of Snph, likely in Basket axon collaterals around PC soma. GFP-OMM is driven by the Cre-driver lines introduced in **a**. Arrowhead, nuclear signal. Images in **a** and **d-f** show representative results from $n=3$ independent experiments. Scale bars: $20 \mu\text{m}$ (**a,d-f**) ($10 \mu\text{m}$ in insets). A, astrocyte, GCL, ganule cell layer; ML, molecular layer; PCL, Purkinje cell layer.

changes obtained by mass spectrometry using western blot quantification for a subset of candidates (Supplementary Fig. 10). In seven cases, no confirmation was achieved because of antibody quality. Some of the validated candidates, especially in astrocytes (Fig. 3f), represent mitochondrial proteins with previous cell-type-specific annotation, such as glycine dehydrogenase (Gldc)²⁰, sideroflexin-5 (Sfxn5)²¹ and monoamine-decarboxylase B (MaoB), which is targeted in positron-emission tomography as an astrocyte tracer²². Notably, the astrocytic mitochondrial proteome contained a substantial enrichment of peroxisomal proteins (Supplementary Figs. 7e,f and 9c), some of which are known to have dual targeting (for example, catalase)²³ or tether to mitochondria (for example, Eci2 (ref. 24) and Pex11b (ref. 25)). In neurons, we expected to identify Snph, a protein involved in regulating mitochondrial distribution and generally believed to be enriched on axonal mitochondria¹⁹. Indeed, in line with our proteomics, we confirmed only weak signals in PC and GC mitochondria; however, we observed prominent mitochondrial labeling in Basket axon collaterals synapsing onto PC somata, hence forming the pinceau organization (Fig. 3d and Supplementary Fig. 9a). In some instances, differentially expressed paralogs were detected between cell types (for example, adenylate kinase 4 (Ak4) versus Ak3; glutaminase (Gls) versus Gls2; Fig. 3e,f). In addition, we observed two forms for Ociad2, a non-*MitoCarta* protein dually assigned to mitochondria and endosomes in a recent publication²⁶. A C-terminal antibody confirmed our proteomic prediction of enrichment in PC mitochondria, whereas an amino-terminal antibody showed enrichment in GC (Supplementary Fig. 11). Surprisingly, we identified cell-type-specific enrichment of mitochondrial proteins for which we expected ubiquitous expression, for example, the mitochondrial calcium uniporter (Mcu)^{27,28} and its regulators in GC. Similarly, Rmdn3 (also known as PTPIP51), a tether involved in calcium handling²⁹ and lipid transfer³⁰ between the endoplasmic reticulum (ER) and mitochondria, was enriched in PC. Altogether, our validated group of cell-type-specific mitochondrial proteins supports the notion that, depending on cell type, mitochondria play diverse roles in metabolism, calcium handling and organelle communication.

Markers reveal cell-type-specific mitochondrial changes in mouse and human pathology. Next, we wanted to explore whether the identified markers could be used to analyze cell-type-specific mitochondria in human pathology. To generalize their applicability, we tested a subset in two other CNS regions, cortex and spinal cord. Indeed, we observed the characteristic pattern of neuronal and astrocytic mitochondria coinciding with cell-type-specific labeling (Fig. 4a and Supplementary Fig. 12). We then applied these markers to tissue from mouse models of Alzheimer's disease (APPPS1 mice) and amyotrophic lateral sclerosis (SOD^{G93A} mice), conditions for which mitochondrial contributions have previously been claimed⁴, but the differential roles of neurons versus astrocytes are still debated³¹. Indeed, the introduced markers showed pathological changes in mitochondrial distribution and shape. For example, they revealed reduced density of neuronal, and to a lesser degree glial, mitochondria around amyloid plaques in the APPPS1 mouse model (Fig. 4b and Supplementary Fig. 13a,b). Similarly, we found pronounced changes in neuronal mitochondria in 3-month-old SOD^{G93A} mice, which were not detectable in astrocytes (Fig. 4d and Supplementary Fig. 14a). Importantly, we confirmed the expression pattern of our mitochondrial markers in human tissues (Fig. 4a and Supplementary Fig. 15) and performed immunofluorescence stainings on human cortex of patients with Alzheimer's disease and human spinal cord affected by amyotrophic lateral sclerosis (Fig. 4c,e and Supplementary Figs. 13c and 14b). These stainings corroborated the changes observed in animal models, thus confirming that the *MitoTag* profiling used in this study identified suitable markers to study cell-type-specific mitochondrial pathology in human disease.

Fatty acids are more efficiently metabolized by astrocytic than neuronal mitochondria. To further explore mitochondrial diversity on the functional level, we performed pathway analysis between neuronal and astrocytic mitochondria, and detected an enrichment of enzymes involved in mitochondrial beta-oxidation (Fig. 5a and Supplementary Fig. 7e). However, the brain is often assumed to rely on glucose and lactate for energy production, rather than lipids³². Still, neural cells appear to respire on fatty acids under certain conditions³³ with important functional implications, for example, in stem cell proliferation³⁴. Despite this, and even though previous bioinformatics analysis has predicted astrocytic beta-oxidation³⁵, it remains controversial whether under steady-state conditions neural cells are fully equipped to perform long-chain fatty acids respiration. Guided by our proteomic profiling, we addressed this question by first confirming the astrocytic enrichment of two enzymes involved in beta-oxidation by immunofluorescence staining, short-chain-specific acyl-coenzyme A dehydrogenase (Acads; Fig. 3f and Supplementary Fig. 9d) and carnitine palmitoyltransferase 1a (Cpt1a; Fig. 5b), a rate-limiting enzyme in long-chain fatty acids oxidation. Second, we used our approach to compare oxygen consumption rates of in situ isolated cell-type-specific mitochondria on the C16-fatty acid, palmitoyl-carnitine (Fig. 5c and Supplementary Fig. 16). We chose a substrate that is preferentially metabolized in mitochondria as a result of its carbon chain length and carnitine pre-conjugation, because astrocytic mitochondria appear to engage selectively with peroxisomes based on our proteomic profiling (Supplementary Fig. 7e,f). Astrocytic mitochondria performed significantly better than PC-derived mitochondria in coupling efficiency (CE; A versus PC: 1.2-fold; $P=0.03$, one-tailed Welch's t -test; $n=11$ and 10 isolations), respiratory capacity ratio (RCR: 1.6-fold; $P<0.001$; $n=11$ and 9 isolations) and spare capacity ratio (SCR: 1.7-fold; $P<0.001$; $n=9$ isolations). In contrast, selective respiration via complex I and II did not differ significantly (Fig. 5d,e and Supplementary Fig. 16).

Mcu mediates calcium uptake in granule cell mitochondria in contrast with Purkinje cells. Mitochondrial calcium influx is mediated via the long-elusive channel Mcu^{27,28} and its interactors. Strikingly, this pathway seems nonessential for cellular survival based on global Mcu deletion in outbred CD1 mice, whereas on inbred C57BL/6 background deletion is lethal³⁶. Furthermore, certain tissues differentially regulate Mcu function³⁷. We were therefore intrigued to find in our proteomic profiling that GC abundantly express the Mcu complex (Fig. 6a), whereas its protein levels are comparably lower in astrocytes and especially PC. We evaluated this by immunofluorescence stainings (Fig. 6b) and western blot analysis (Fig. 6c), and found a reduction of Mcu levels to 31.7% in PC and 45.4% in astrocytic mitochondria compared with GC mitochondria. Given these differences, we analyzed calcium uptake capacity of isolated, cell-type-specific mitochondria (Fig. 6d,e). Whereas GC mitochondria efficiently buffered calcium in a Mcu-dependent manner (that is, Ru360 sensitive), PC mitochondria showed a significantly (Fig. 6e; $P=0.0018$) reduced calcium buffering capacity (GC versus PC: $P=0.0018$, analysis of variance (ANOVA) with post hoc testing; $n=5$ and 7 isolations). Cell-type-specific ablation of Mcu in GC (Fig. 6f,g) abolished their mitochondrial calcium uptake capacity (Fig. 6h,i). Once more, these data demonstrate the diversity of mitochondria even for fundamental functions and between neuronal subtypes, and underscore the potential of the *MitoTag* approach to analyze mitochondrial functions and signaling pathways in the context of individual cell types.

Rmdn3 mediates ER-mitochondria juxtapositions in Purkinje cells. A central aspect of mitochondrial function is communication with other organelles, for example, via contact sites³⁸. Rmdn3 is an established tether between the ER and mitochondria involved in calcium²⁹ and lipid transfer³⁰. In our proteomic profiling, we found

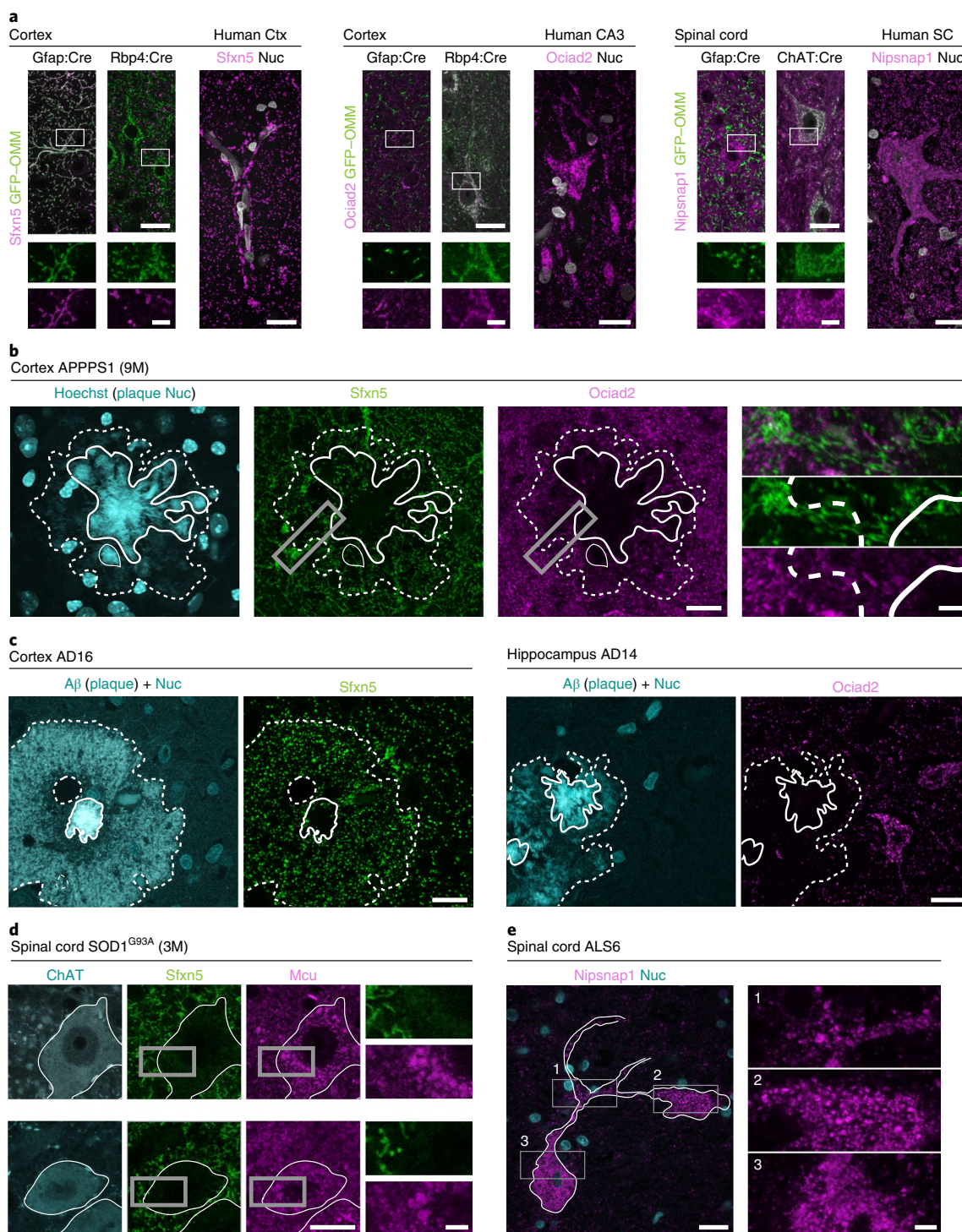


Fig. 4 | Cell-type-specific mitochondrial markers are conserved within the CNS and across species, and they enable mitochondrial studies under pathological conditions. **a**, Cell-type-specific mitochondrial markers are conserved across the cortex (Ctx) and spinal cord (SC) as shown for Sfxn5 (astrocytic), Ociad2 (neuronal subtype) and Nipsnap1 (neuronal) using tissue from *MitoTag* mice crossed to Gfap:Cre, Rbp4:Cre and ChAT:Cre-driver lines (see Supplementary Fig. 12), and also in corresponding human tissue (right panels within tissue group; see Supplementary Fig. 15). **b–e**, Mitochondrial markers in murine disease models and postmortem tissue from patients with Alzheimer’s disease (AD) and amyotrophic lateral sclerosis (ALS). **b**, Around amyloid plaques (Hoechst, cyan), astrocytic mitochondria (Sfxn5, green) are excluded from the core region (white line), whereas neuronal mitochondria (Ociad2, magenta) show an altered density within diffuse parts of the plaques (dashed line; see Supplementary Fig. 13a). **c**, Postmortem cortex and hippocampus tissues from patients with AD confirm the distribution changes seen in mouse (see Supplementary Fig. 13c). Amyloid plaques are stained with amyloid-β antibody, and the channel was merged with DAPI (Nuc). **d**, In presymptomatic SOD1^{G93A} mice, neuronal mitochondria (Mcu, magenta) are morphologically altered, whereas astrocytic mitochondria (Sfxn5, green) appear normal (see Supplementary Fig. 14a). **e**, In human postmortem ALS spinal cord, similar mitochondrial phenotypes are observed in remaining neurons (Nipsnap1; see Supplementary Fig. 14b; cell outline constructed from z-stack). Data from mouse tissue are representative of $n=2$ independent experiments. Data from human tissue are representative of one experiment performed in $n \geq 3$ cases. Case identifiers are given after disease names. Scale bars: 20 μm (**a–e**) (5 μm in insets). 9M/3M, 9 months and 3 months; ChAT, choline acetyltransferase; Nuc, nuclear counterstain.

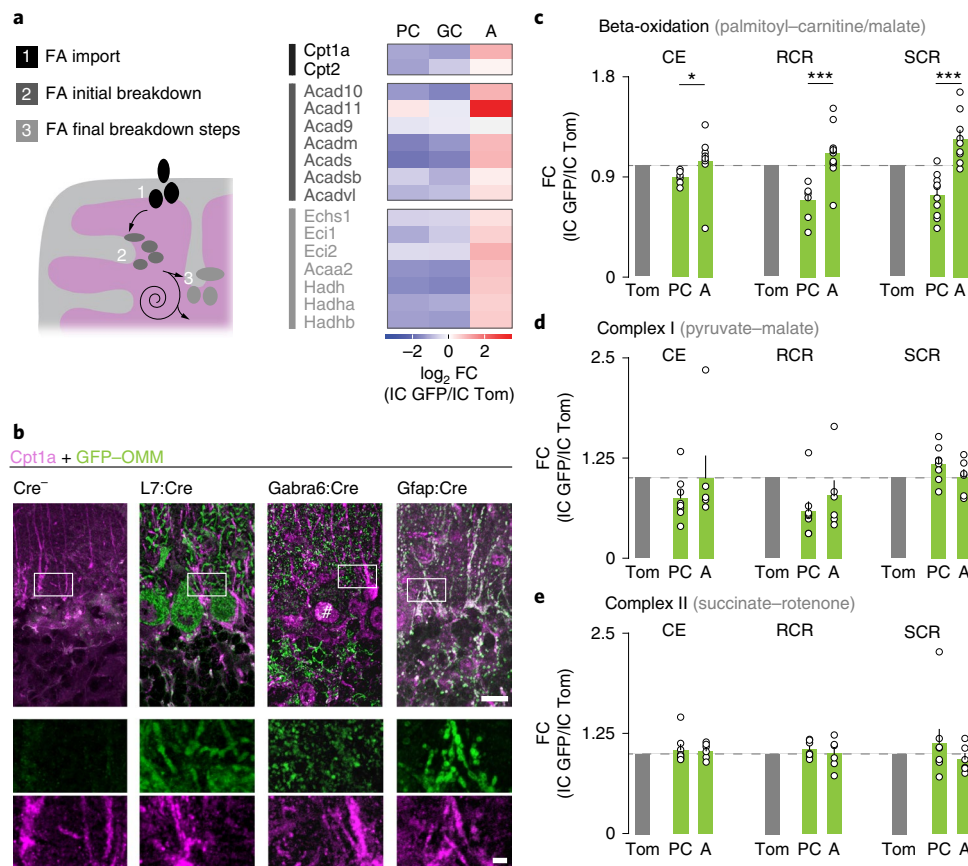


Fig. 5 | Astrocytic mitochondria metabolize long-chain fatty acids more efficiently than neurons. **a**, Localization of the three steps of beta-oxidation in mitochondria: fatty acid (FA) import (1), initial breakdown (2) and final breakdown (3). Heat map showing cell-type-specific protein changes for enzymes involved in beta-oxidation as average log₂ FC (IC GFP/IC Tom). **b**, Immunostaining for Cpt1a (magenta) colocalizes with astrocytic mitochondria in the cerebellum (right; Gfap:Cre/GFP-OMM, green). Staining is additionally shown in tissue from Cre⁻, L7:Cre/GFP-OMM and Gabra6:Cre/GFP-OMM mice. Hash sign (#) indicates nuclear signal of Cpt1a. Images show representative results from *n* = 3 independent experiments. **c–e**, Bioenergetic parameters derived from oxygen consumption measurements of immunocaptured mitochondria from PC (L7:Cre/GFP-OMM) or astrocytes (Gfap:Cre/GFP-OMM) in the presence of different substrates. **c**, All parameters under palmitoyl–carnitine/malate are significantly higher in astrocytic mitochondria (CE: *P* = 0.0436; RCR: *P* = 0.0001; SRC: *P* < 0.0001, one-tailed, unpaired Welch’s *t*-test; *n* ≥ 9 isolations). **d,e**, Parameters under pyruvate–malate (**d**) and succinate–rotenone (**e**) do not show any significant difference. For comparison, parameters are normalized to corresponding IC Tom value (gray bars; see Supplementary Fig. 16 for non-normalized values). Dot plot: mean ± s.e.m. Scale bars: 25 μm (**c**) (5 μm in insets). CE, coupling efficiency; RCR, respiratory capacity ratio; SCR, spare capacity ratio.

this OMM protein³⁹ to be enriched in PC mitochondria by 3.5-fold over GC mitochondria and 4.1-fold over astrocytic mitochondria. Previous reports established the interaction of Rmdn3 with ER-membrane proteins, namely VAPB (an amyotrophic lateral sclerosis-associated protein)²⁹ and ORP5/8 (ref. 30). First, we confirmed by immunofluorescence staining that Rmdn3 is highly enriched in PC mitochondria (Fig. 7a). Next, we tested the functional prediction that PC possess more extensive ER–mitochondria contacts compared with GC and astrocytes. Indeed, using ultrastructural analysis, we found that organelle contacts in PC somata were 6.2-fold more enriched compared with GC somata and 2.6-fold more extensive compared with neighboring astrocytes (contacts ≤ 30 nm in distance: 37.7% PC versus 6.1% GC/14.5% astrocytes; in all cases, *P* < 0.0001, Kruskal–Wallis with post hoc testing; *n* = 160, 134 and 120 mitochondria from two mice; Fig. 7b and Supplementary Fig. 17a). Finally, using a knockout mouse model, we confirmed that these juxtapositions are affected by Rmdn3 levels. These mice showed a gene dose-dependent protein loss in cerebellum by western blot and immunofluorescence analysis (Fig. 7c,d), even though some nonspecific bands and residual nonneuronal staining persisted. Ultrastructural appraisal demonstrated a reduction of

ER–mitochondria contacts in PC somata (contacts ≤ 30 nm in distance: +/+, 37.1%; +/-, 28.3%; -/-, 19.6%; +/+ versus -/-: *P* < 0.0001, +/+ versus +/-: *P* = 0.0022, +/- versus -/-: *P* = 0.0016, ANOVA with post hoc testing; *n* = 12, 8 and 14 cells from two to three mice; Fig. 7e and Supplementary Fig. 17b), whereas contacts in astrocytes were not significantly altered.

Discussion

Here, we describe a versatile approach to obtain intact cell-type-specific mitochondria from complex tissues. This approach allows for functional and ‘omics’-level analysis of mitochondria derived from any cell type during development, physiology and disease. We demonstrate this by comparing the mitochondrial proteomes of the principal inhibitory and excitatory neurons, as well as of the major glial cell type in the mouse cerebellum.

Compared with other methods that explore the molecular composition of mitochondria, our approach has a number of advantages. First, mice of all ages and genotypes can be used, enabling studies of aging-related changes or disease models, which for many cell types are not possible with cell culture- or tissue dissociation-based approaches. Second, in cells with extended morphology,

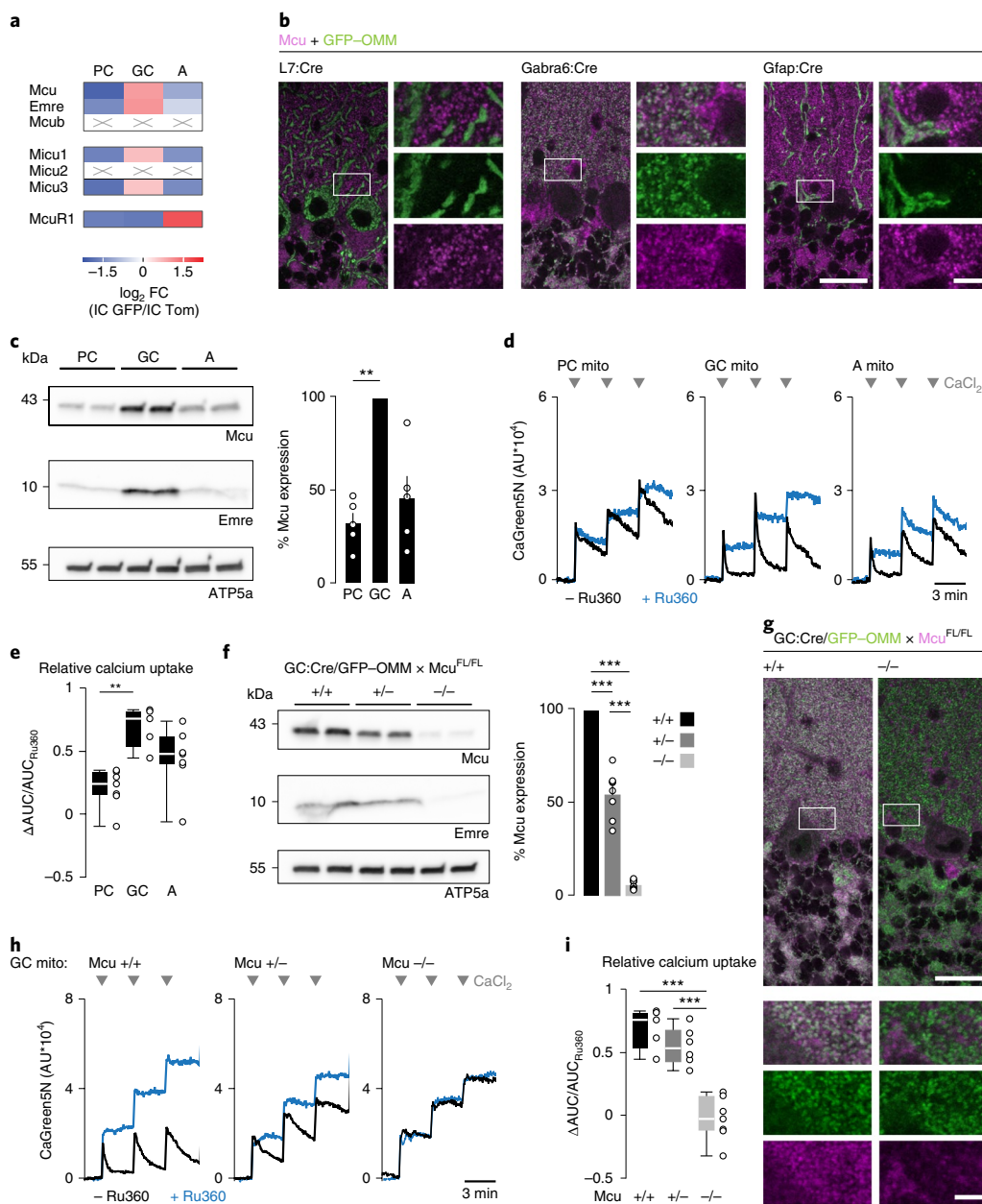


Fig. 6 | Granule cell mitochondria robustly buffer calcium via Mcu in contrast with Purkinje cell mitochondria. **a**, Heat map showing cell-type-specific protein changes for known components of the Mcu complex as average \log_2 FC (IC GFP/ IC Tom). **b**, Immunostaining for Mcu (magenta) colocalizes with GC mitochondria in the cerebellum (middle; Gabra6:Cre/GFP-OMM, green). Staining is additionally shown in tissue from L7:Cre/GFP-OMM and Gabra6:Cre/GFP-OMM mice. **c**, Validation of Mcu levels in mitochondria from PC, GC and astrocytes (A) using western blot analysis. Cell-type-specific mitochondria (IC GFP) were analyzed probing for Mcu, Emre and ATP5a. Graphs show quantification of Mcu levels relative to mitochondrial content (PC versus GC: $P=0.0047$, one-way Friedman's test with post hoc testing; $n=5$ experiments from four mice per group). **d**, Calcium uptake of immunocaptured mitochondria from the three cell types in the absence (black line) or presence (blue line) of Ru360, an Mcu inhibitor. Calcium uptake is shown as the decrease in fluorescence of the extra-mitochondrial calcium indicator GaGreen-5N after the application of $20\ \mu\text{M}$ CaCl_2 . Traces are from one experiment performed with all cell types and quantified in **e**. **e**, Mitochondria. **e**, Quantification of calcium uptake shown in **d** is related to the first pulse of CaCl_2 , given as $\Delta\text{AUC}/\text{AUC}_{\text{Ru360}}$ (GC versus PC: $P=0.0018$, ANOVA with post hoc testing; $n\geq 5$ isolations). Datasets of GC mitochondria and +/- mitochondria in **i** are identical. **f**, Validation of Mcu knockout in mitochondria from GC (Gabra6:Cre/GFP-OMM \times Mcu^{FL/FL}) using western blot analysis. GC-specific mitochondria (IC GFP) were analyzed probing for Mcu, Emre and ATP5a. Graphs show quantification of Mcu levels relative to mitochondrial content ($P<0.0001$ for all comparisons, one-way restricted maximum likelihood (REML) with post hoc testing; $n=6-10$ mice). **g**, Immunostaining for Mcu (magenta) in Gabra6:Cre/GFP-OMM \times Mcu^{FL/FL} background shows depletion of Mcu signal in GFP-OMM-labeled GC mitochondria (right). Other cell types are not affected and show Mcu expression. **h**, Calcium uptake of immunocaptured mitochondria from GCs deficient in Mcu (+/+, +/- and -/-) in the absence (black line) or presence (blue line) of Ru360 with application of $20\ \mu\text{M}$ CaCl_2 . Traces are from one experiment performed with all genotypes and quantified in **i**. **i**, Quantification of calcium uptake related to the first pulse of CaCl_2 given as $\Delta\text{AUC}/\text{AUC}_{\text{Ru360}}$ (+/+ versus -/-: $P<0.0001$; +/- versus -/-: $P<0.0001$, one-way ANOVA with post hoc testing; $n\geq 5$ isolation). Datasets of +/- mitochondria and GC mitochondria in **e** are identical. Dot plot: mean \pm s.e.m.; box plot: median, quartile 1-quartile 3, maximum and minimum values. Images in **b** and **g** show representative results from $n=3$ independent experiments. Scale bars: $25\ \mu\text{m}$ (**b,g**) ($5\ \mu\text{m}$ in insets).

mitochondria from all compartments can be obtained. We illustrate this by capturing axonal mitochondria from cholinergic forebrain projections (Supplementary Figs. 1b and 5d). Importantly, the systematic exploration of compartment-specific mitochondria is possible with the *MitoTag* approach, for example, from neurons that project to different brain regions. Although still in its infancy, this research area will probably yield fundamental insights into the multifaceted role of neuronal mitochondria³ given the recent insights into the role of local translation for mitochondrial homeostasis at synapses and in axons⁴⁰, as well as into compartment-specific regulation of mitochondrial dynamics⁴¹. Third, whereas transcriptomes allow exploring the regulation of mitochondrial gene expression³⁵, mitochondrial proteomes are shaped by several layers of regulation³ and hence are even less predictable from transcriptomes than global cellular proteomes⁹. Our direct proteomic approach circumvents this limitation. Fourth, our approach can yield proteins that are uncharacterized or only transiently associated with mitochondria that would be otherwise overlooked by methods relying on prior knowledge of mitochondrial localization. Fifth, in contrast

with methods that are based on the affinity purification of labeled proteins from cell types, for example, BONCAT⁴² or APEX⁴³, our approach provides the intact and functional organelle for correlated analysis of the mitochondrial genome or transcriptome¹³, as well as

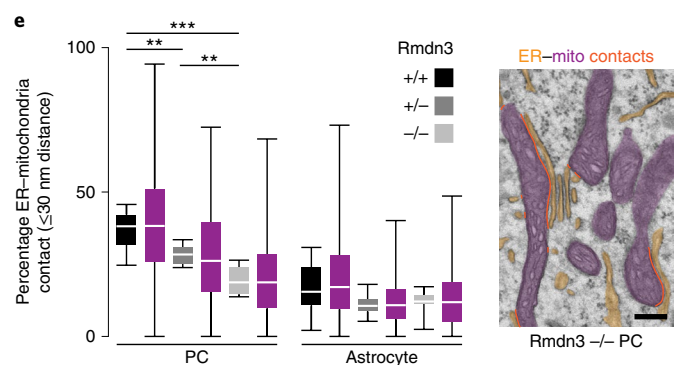
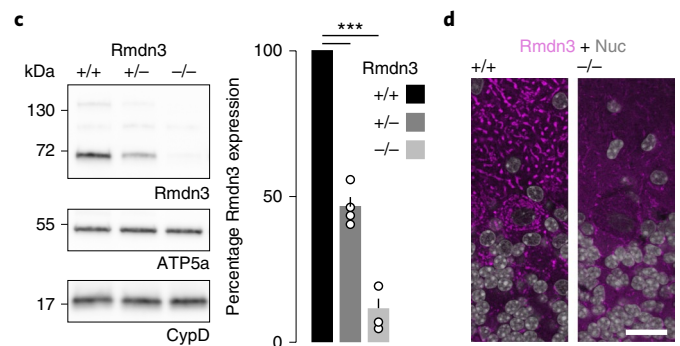
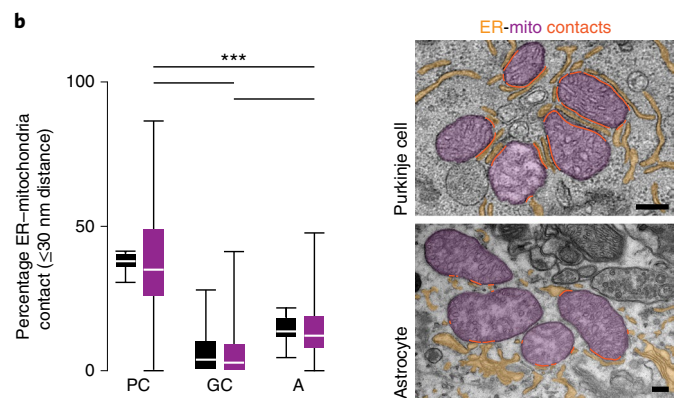
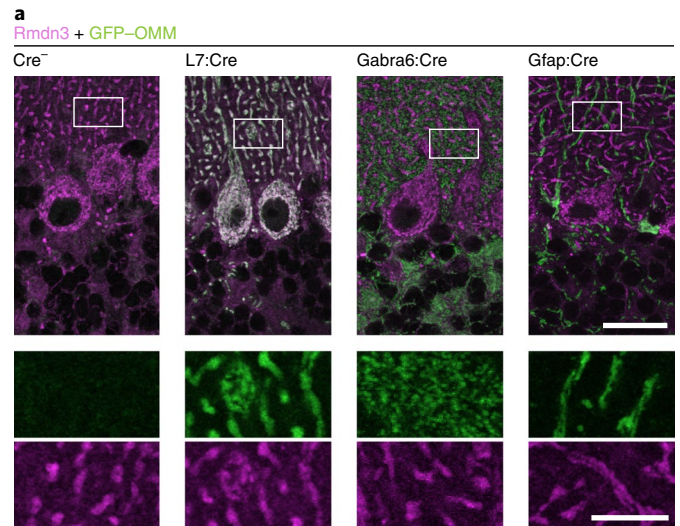
Fig. 7 | Rmdn3 mediates close ER-mitochondria juxtapositions in Purkinje cells.

a, Immunostaining for Rmdn3 (magenta) colocalizes with PC mitochondria in the mouse cerebellum (second panels from left; L7:Cre/GFP-OMM, green). Staining is additionally shown in tissue from Cre⁻, Gfap:Cre/GFP-OMM and Gabra6:Cre/GFP-OMM mice. Images show representative results from n=3 independent experiments.

b, Ultrastructural analysis of ER-mitochondria (mito) proximity in wild-type cerebellum reveals the degree of proximity of ER (orange) to mitochondria (magenta) in the cytoplasm of PC, GC and adjoining astrocytes. Note differing scale bar sizes because of mitochondrial size. The contact frequency between organelles is shown as % mitochondrial perimeter in distance ≤ 30 nm (red lines) and illustrated as box plot (median, quartile 1-quartile 3, maximum and minimum values; black) using cells per cell type (n = 10, 74 and 16 cells from two mice; increased n for GC because of cell morphology) and as box plot (median, quartile 1-quartile 3, maximum and minimum values; magenta) using mitochondria as statistical entities (P < 0.0001 in all comparisons, one-way Kruskal-Wallis test with post hoc testing; n ≥ 120 mitochondria per cell type from two mice).

c, d, Rmdn3-knockout mice show a gene dose-dependent reduction in Rmdn3 protein levels in the cerebellum. **c**, Total lysate from the cerebellum of wild-type (+/+), heterozygous (+/-) and knockout (-/-) mice was analyzed via western blot probing for Rmdn3 (size: 51 kDa and > 130 kDa) and mitochondrial proteins (ATP5a, CypD). Graphs (mean ± s.e.m. with individual points) show quantification of Rmdn3 levels relative to mitochondrial content (+/+ versus -/-: P = 0.0001, +/+ versus +/-: P = 0.0005, two-tailed, paired t-test; n = 4 mice). **d**, Immunostaining for Rmdn3 (magenta) in wild-type (left; +/+) and knockout (right; -/-) cerebellum shows loss of mitochondrial pattern in PC. The weak residual signal in astrocytic mitochondria is because of imperfect specificity of the antibody for the canonical form (52 kDa) of Rmdn3 (see Supplementary Fig. 18c). Images show representative results from n = 2 independent experiments.

e, Ultrastructural analysis of ER-mitochondria proximity in Rmdn3-knockout cerebellum reveals reduced contact frequency (ER, orange; mitochondria, magenta; contact, red lines) in the cytoplasm of PC (electron micrograph). Box plot (median, quartile 1-quartile 3, maximum and minimum values; gray tones) shows the decrease in contact frequency between organelles based on cells as statistical entities (≤ 30 nm distance; +/+ versus -/-: P < 0.0001, +/+ versus +/-: P = 0.0022, +/- versus -/-: P = 0.0016, one-way ANOVA with post hoc testing; n ≥ 8 cells from two to three mice) in PC, but not in astrocytes (+/+ versus -/-: P = 0.17, +/+ versus +/-: P = 0.12; n ≥ 10 cells from 2-3 mice) and box plot (median, quartile 1-quartile 3, maximum and minimum values; magenta) shows the population of mitochondria per genotype and cell type (n ≥ 105 mitochondria from two to three mice). Scale bars: 25 μm (**a**) (5 μm in insets); 200 nm (**b,e**); 20 μm (**d**). Nuc, nuclear counterstain.



of mitochondrial functions, for example, respiration, calcium handling, ROS production or metabolism⁴⁴. This is further aided by the fluorescent tag, which allows in situ observation, and the bulk immunocapture approach, which is relatively swift and gentle, an important feature for functional investigations¹¹. Indeed, during revision of this article, a metabolomic analysis of hepatocytes from mouse liver was reported using a related approach⁴⁴.

When applied to the adult cerebellum, our approach yielded a number of insights. First, it revealed profound mitochondrial diversity among cell types, with a substantial part of the annotated mitochondrial proteome (~15%) being differentially regulated among the investigated cell types (Fig. 3b). Second, our verified cell-type-specific mitochondrial proteins provided a set of in situ markers to characterize the distribution and morphology of mitochondria in specific neural cell types across developmental stages and brain regions. Third, these markers allow resolving of cell-type-specific mitochondrial changes under pathological conditions, both in mouse models and human tissue, because of their conservation across species (Supplementary Fig. 15). Especially in human tissue, this has only been possible for cellular compartments that are large enough to be resolved by light microscopy⁴⁵, or by using electron microscopy, which is cumbersome and highly susceptible to postmortem changes. We highlight this application by demonstrating mitochondrial morphology in neurons and astrocytes around amyloid- β plaques in APPPS1 mice and in the spinal cord of SOD1^{G93A} mice, as well as in corresponding human autopsy specimen (Fig. 4b–e). Fourth, pathway analysis of our cerebellar proteomes resulted in clear predictions for differentially regulated metabolic pathways (Supplementary Fig. 7e), which we could directly confirm by demonstrating efficient beta-oxidation in immunocaptured astrocytic mitochondria (Fig. 5c). Fifth, chiming with the astrocyte's ability to respire on fatty acids, we observed an enrichment of peroxisomal proteins in immunocaptured mitochondria from astrocytes (Supplementary Fig. 7e,f). Because peroxisomes are another important compartment for lipid metabolism and engage intimately with mitochondria, this interaction might enhance glial use of lipids and the exchange of proteins between mitochondria and peroxisomes, for example, as part of peroxisome biogenesis⁴⁶. Sixth, our proteomic profiling predicted candidates that mediate cell-type-specific regulation of organelle contacts. For instance, we found a recently identified mitochondria-peroxisome tether, Pex11B (ref. 25), enriched in astrocytic mitochondria. Similarly, we identified Rmdn3 enriched in PC mitochondria, which mediates ER–mitochondria contact sites (Fig. 7). Seventh, the enrichment of Rmdn3 fits well with independent observations, indicating unique intracellular calcium handling mechanisms in PC related to this cell's distinct morphology, firing pattern and synaptic plasticity⁴⁷. In contrast, mitochondrial calcium handling in GC seems to be enhanced by strong expression of the Mcu complex. Indeed, ex vivo comparison of mitochondria from these two neuronal subtypes demonstrated a robust difference in this fundamental calcium entry path (Fig. 6). Other cell-type-specific regulation of mitochondrial calcium handling has been observed in excitable tissues^{28,48}, regulated either by tissue-specific expression of Mcu components (Mcu1–3) or by posttranslational modifications (for example, redox state)⁴⁹. The low expression of the Mcu complex in PC thus matches intriguingly well to the enhanced ER–mitochondria contacts mediated by Rmdn3, but could also relate to the high levels of cytoplasmic calcium buffers in PC, for example, parvalbumin which in other cells antagonize Mcu expression⁵⁰.

Overall, our data reveal a hitherto unappreciated cell-type-specific regulation of even basic mitochondrial functions in the CNS. Thus, this approach clearly demonstrates that cell-type-specific molecular diversity of mitochondria not only serves homeostatic needs to preserve essential functions in cells of different

geometries³, but this diversity also imbues mitochondria with special properties that contribute to the unique function of a given cell type in the healthy brain and its selective vulnerability during disease. Our data prove that underneath the initial perception of mitochondria as rather uniform and autonomous organelles lies a layer of profound cell-type-specific mitochondrial biology that we are only starting to appreciate. Given the startling tissue and cell type specificity of many pathologies involving mitochondria⁵¹ and the increasing number of roles ascribed to mitochondria as a signaling hub, the *MitoTag* approach provides a valuable tool to recognize mitochondria fully as the multifaceted organelles that they are.

Online content

Any methods, additional references, Nature Research reporting summaries, source data, statements of code and data availability and associated accession codes are available at <https://doi.org/10.1038/s41593-019-0479-z>.

Received: 26 September 2018; Accepted: 25 July 2019;
Published online: 9 September 2019

References

- MacIver, N. J., Michalek, R. D. & Rathmell, J. C. Metabolic regulation of T lymphocytes. *Annu. Rev. Immunol.* **31**, 259–283 (2013).
- Chen, H. & Chan, D. C. Mitochondrial dynamics in regulating the unique phenotypes of cancer and stem cells. *Cell Metab.* **26**, 39–48 (2017).
- Misgeld, T. & Schwarz, T. L. Mitostasis in neurons: maintaining mitochondria in an extended cellular architecture. *Neuron* **96**, 651–666 (2017).
- Devine, M. J. & Kittler, J. T. Mitochondria at the neuronal presynapse in health and disease. *Nat. Rev. Neurosci.* **19**, 63–80 (2018).
- Nunnari, J. & Suomalainen, A. Mitochondria: in sickness and in health. *Cell* **148**, 1145–1159 (2012).
- West, A. P., Shadel, G. S. & Ghosh, S. Mitochondria in innate immune responses. *Nat. Rev. Immunol.* **11**, 389–402 (2011).
- Pagliarini, D. J. et al. A mitochondrial protein compendium elucidates complex I disease biology. *Cell* **134**, 112–123 (2008).
- Shigeoka, T. et al. Dynamic axonal translation in developing and mature visual circuits. *Cell* **166**, 181–192 (2016).
- Ghazalpour, A. et al. Comparative analysis of proteome and transcriptome variation in mouse. *PLoS Genet.* **7**, e1001393 (2011).
- Heiman, M. et al. A translational profiling approach for the molecular characterization of CNS cell types. *Cell* **135**, 738–748 (2008).
- Chen, W. W., Freinkman, E., Wang, T., Birsoy, K. & Sabatini, D. M. Absolute quantification of matrix metabolites reveals the dynamics of mitochondrial metabolism. *Cell* **166**, 1324–1337.e1311 (2016).
- Abu-Remaileh, M. et al. Lysosomal metabolomics reveals V-ATPase- and mTOR-dependent regulation of amino acid efflux from lysosomes. *Science* **358**, 807–813 (2017).
- Ahier, A. et al. Affinity purification of cell-specific mitochondria from whole animals resolves patterns of genetic mosaicism. *Nat. Cell Biol.* **20**, 352–360 (2018).
- Roh, H. C. et al. Simultaneous transcriptional and epigenomic profiling from specific cell types within heterogeneous tissues in vivo. *Cell Rep.* **18**, 1048–1061 (2017).
- Hornig-Do, H. T. et al. Isolation of functional pure mitochondria by superparamagnetic microbeads. *Anal. Biochem.* **389**, 1–5 (2009).
- Meeusen, S., McCaffery, J. M. & Nunnari, J. Mitochondrial fusion intermediates revealed in vitro. *Science* **305**, 1747–1752 (2004).
- Sharma, K. et al. Cell type- and brain region-resolved mouse brain proteome. *Nat. Neurosci.* **18**, 1819–1831 (2015).
- Calvo, S. E., Clauser, K. R. & Mootha, V. K. MitoCarta2.0: an updated inventory of mammalian mitochondrial proteins. *Nucl. Acids Res.* **44**, D1251–D1257 (2016).
- Kang, J. S. et al. Docking of axonal mitochondria by syntaphilin controls their mobility and affects short-term facilitation. *Cell* **132**, 137–148 (2008).
- Sato, K., Yoshida, S., Fujiwara, K., Tada, K. & Tohyama, M. Glycine cleavage system in astrocytes. *Brain Res.* **567**, 64–70 (1991).
- Miyake, S. et al. Identification and characterization of a novel mitochondrial tricarboxylate carrier. *Biochem. Biophys. Res. Commun.* **295**, 463–468 (2002).
- Fowler, J. S. et al. Monoamine oxidase: radiotracer development and human studies. *Methods* **27**, 263–277 (2002).
- Petrova, V. Y., Drescher, D., Kujumdzieva, A. V. & Schmitt, M. J. Dual targeting of yeast catalase a to peroxisomes and mitochondria. *Biochem. J.* **380**, 393–400 (2004).

24. Fan, J., Li, X., Issop, L., Culty, M. & Papadopoulos, V. ACBD2/ECI2-mediated peroxisome-mitochondria interactions in Leydig cell steroid biosynthesis. *Mol. Endocrinol.* **30**, 763–782 (2016).
25. Shai, N. et al. Systematic mapping of contact sites reveals tethers and a function for the peroxisome-mitochondria contact. *Nat. Commun.* **9**, 1761 (2018).
26. Sinha, S., Bheemsetty, V. A. & Inamdar, M. S. A double helical motif in OCIAD2 is essential for its localization, interactions and STAT3 activation. *Sci. Rep.* **8**, 7362 (2018).
27. Baughman, J. M. et al. Integrative genomics identifies MCU as an essential component of the mitochondrial calcium uniporter. *Nature* **476**, 341–345 (2011).
28. De Stefani, D., Raffaello, A., Teardo, E., Szabó, I. & Rizzuto, R. A forty-kilodalton protein of the inner membrane is the mitochondrial calcium uniporter. *Nature* **476**, 336–340 (2011).
29. De Vos, K. J. et al. VAPB interacts with the mitochondrial protein PTPIP51 to regulate calcium homeostasis. *Hum. Mol. Genet.* **21**, 1299–1311 (2012).
30. Galmes, R. et al. ORP5/ORP8 localize to endoplasmic reticulum-mitochondria contacts and are involved in mitochondrial function. *EMBO Rep.* **17**, 800–810 (2016).
31. Di Giorgio, F. P., Boulting, G. L., Bobrowicz, S. & Eggan, K. C. Human embryonic stem cell-derived motor neurons are sensitive to the toxic effect of glial cells carrying an ALS-causing mutation. *Cell Stem Cell* **3**, 637–648 (2008).
32. Schönfeld, P. & Reiser, G. Why does brain metabolism not favor burning of fatty acids to provide energy? Reflections on disadvantages of the use of free fatty acids as fuel for brain. *J. Cereb. Blood Flow. Metab.* **33**, 1493–1499 (2013).
33. Ebert, D., Haller, R. G. & Walton, M. E. Energy contribution of octanoate to intact rat brain metabolism measured by ¹³C nuclear magnetic resonance spectroscopy. *J. Neurosci.* **23**, 5928–5935 (2003).
34. Knobloch, M. et al. A fatty acid oxidation-dependent metabolic shift regulates adult neural stem cell activity. *Cell Rep.* **20**, 2144–2155 (2017).
35. Eraso-Pichot, A. et al. GSEA of mouse and human mitochondriomes reveals fatty acid oxidation in astrocytes. *Glia* **66**, 1724–1735 (2018).
36. Harrington, J. L. & Murphy, E. The mitochondrial calcium uniporter: mice can live and die without it. *J. Mol. Cell. Cardiol.* **78**, 46–53 (2015).
37. Paillard, M. et al. Tissue-Specific mitochondrial decoding of cytoplasmic Ca(2+) signals is controlled by the stoichiometry of MICU1/2 and MCU. *Cell Rep.* **18**, 2291–2300 (2017).
38. Eisenberg-Bord, M., Shai, N., Schuldiner, M. & Bohnert, M. A tether is a tether: tethering at membrane contact sites. *Dev. Cell* **39**, 395–409 (2016).
39. Lv, B. F. et al. Protein tyrosine phosphatase interacting protein 51 (PTPIP51) is a novel mitochondria protein with an N-terminal mitochondrial targeting sequence and induces apoptosis. *Apoptosis* **11**, 1489–1501 (2006).
40. Rangaraju, V., Lauterbach, M. & Schuman, E. M. Spatially stable mitochondrial compartments fuel local translation during plasticity. *Cell* **176**, 73–84.e15 (2019).
41. Lewis, T. L. Jr., Kwon, S. K., Lee, A., Shaw, R. & Polleux, F. MFF-dependent mitochondrial fission regulates presynaptic release and axon branching by limiting axonal mitochondria size. *Nat. Commun.* **9**, 5008 (2018).
42. Alvarez-Castelao, B. et al. Cell-type-specific metabolic labeling of nascent proteomes in vivo. *Nat. Biotechnol.* **35**, 1196–1201 (2017).
43. Chen, C. L. et al. Proteomic mapping in live drosophila tissues using an engineered ascorbate peroxidase. *Proc. Natl Acad. Sci. USA* **112**, 12093–12098 (2015).
44. Bayraktar, E. C. et al. MITO-Tag mice enable rapid isolation and multimodal profiling of mitochondria from specific cell types in vivo. *Proc. Natl Acad. Sci. USA* **116**, 303–312 (2019).
45. Kerschensteiner, M., Reuter, M. S., Lichtman, J. W. & Misgeld, T. Ex vivo imaging of motor axon dynamics in murine triangularis sterni explants. *Nat. Protoc.* **3**, 1645–1653 (2008).
46. Sugiura, A., Mattie, S., Prudent, J. & McBride, H. M. Newly born peroxisomes are a hybrid of mitochondrial and ER-derived pre-peroxisomes. *Nature* **542**, 251–254 (2017).
47. Meera, P., Pulst, S. M. & Otis, T. S. Cellular and circuit mechanisms underlying spinocerebellar ataxias. *J. Physiol.* **594**, 4653–4660 (2016).
48. Zaglia, T. et al. Content of mitochondrial calcium uniporter (MCU) in cardiomyocytes is regulated by microRNA-1 in physiologic and pathologic hypertrophy. *Proc. Natl Acad. Sci. USA* **114**, E9006–E9015 (2017).
49. Dong, Z. et al. Mitochondrial Ca²⁺ uniporter is a mitochondrial luminal redox sensor that augments MCU channel activity. *Mol. Cell* **65**, 1014–1028.e1017 (2017).
50. Henzi, T. & Schwaller, B. Antagonistic regulation of parvalbumin expression and mitochondrial calcium handling capacity in renal epithelial cells. *PLoS One* **10**, e0142005 (2015).
51. Suomalainen, A. & Battersby, B. J. Mitochondrial diseases: the contribution of organelle stress responses to pathology. *Nat. Rev. Mol. Cell Biol.* **19**, 77–92 (2018).

Acknowledgements

We thank M. Budak, N. Budak and S. Taskin for animal husbandry and A. Berghofer, A. Graupner, Y. Hufnagel, K. Wullimann and M. Schetterer for technical and administrative support. We thank U. Fünfschilling (Max Planck Institute Göttingen) for providing Gabra6:Cre mice, D. Crane (Griffith University) for the Pex14 antibody and N. Mizushima (Addgene plasmid #38249) for the pMXs-IP GFP-Omp25 plasmid. We are grateful to L. Jiang for help with bioinformatics analyses, Y.-H. Tai for neonatal virus injection and B. Zott for APPPS1 breeding. We thank L. Godinho, M. Schuldiner and O. Schuldiner for reading an earlier version of this article. This work was supported by the Deutsche Forschungsgemeinschaft through the Munich Center for Systems Neurology (SyNergy; grant no. EXC 1010 to A.K., T.K., S.F.L., T.M., F.P. and W.W.); the Center for Integrated Protein Science Munich (grant no. EXC 114 to A.K. and T.M.); the Collaborative Research Centers (CRC870 to T.M., CRC1054 to T.K. and CRC-TR128 to T.K.); research unit grant no. FOR2290 to S.F.L. and research grant no. Mi694/7-1/8-1 to T.M. F.P. and J.W. were supported by the Emmy-Noether program of the Deutsche Forschungsgemeinschaft (grant no. Pe2053/1-1 to F.P.). Further support came from the European Research Council under the European Union's Seventh Framework Program (grant no. FP/2007-2013; European Research Council Grant Agreement nos. CoG 616791 to T.M. and CoG 647215 to T.K.) and the German Center for Neurodegenerative Diseases (DZNE Munich to S.F.L., T.M. and W.W.). L.T. was supported by an EMBO Long-Term Fellowship (no. EMBO ALTF 108-2013). Further support came from the Centers of Excellence in Neurodegeneration and the Helmholtz-Israel Program to S.F.L., the Swiss National Science Foundation and HHS Foundation to D.M., the German Federal Ministry of Education and Research (BMBF) through 'T-B interaction in NMO' to T.K. and 'Mitochondrial endophenotypes of Morbus Parkinson' (grant no. 031A430E) to W.W. A.K. is supported by a Senior Hertie Professorship of Neuroscience. T.M. is supported by the Institute for Advanced Study, Technical University of Munich (Focus Group 'Subcellular Dynamics in Neurons').

Author contributions

C.F., L.T. and T.M. devised the study. L.T., T.M., O.O., R.K. and W.W. designed and generated the *MitoTag* mice, which C.F. and L.T. characterized. C.F. designed the immunocapture protocol (with support from J.W. and F.P.) and performed most of the isolations. S.A.M. and S.F.L. performed sample preparation, mass spectrometry and primary data analysis. C.F. further analyzed the proteomics datasets. L.T. performed bioenergetics measurements and corresponding isolations (with support from J.W. and F.P.). C.F. performed calcium uptake assays (with support from F.P.). C.F., S.H. and T.K. performed and analyzed flow cytometry. C.F. performed western blot analysis and immunofluorescence stainings of candidates. N.S. and C.F. obtained and analyzed electron microscopy data. C.F. characterized the *Rmdn3*^{-/-} and GC-specific *Mcu*^{FL/FL} mouse models. J.H., R.M.K. and A.K. provided pilot experiments for single-cell characterization in the cerebellum. A.K. provided APPPS1 mice. I.W. and D.M. performed immunofluorescence staining on human tissue. C.F., L.T. and T.M. wrote the paper with input from all authors.

Competing interests

The authors declare no competing interests.

Additional information

Supplementary information is available for this paper at <https://doi.org/10.1038/s41593-019-0479-z>.

Reprints and permissions information is available at www.nature.com/reprints.

Correspondence and requests for materials should be addressed to T.M.

Peer review information: *Nature Neuroscience* thanks Robert Friedlander, Daniel McClatchy and the other, anonymous, reviewer(s) for their contribution to the peer review of this work.

Publisher's note: Springer Nature remains neutral with regard to jurisdictional claims in published maps and institutional affiliations.

© The Author(s), under exclusive licence to Springer Nature America, Inc. 2019

Methods

Molecular cloning of GFP–OMM targeting vector for *MitoTag* mouse generation.

The GFP–OMM sequence was derived from the pMXs-IP GFP–Omp25 plasmid, which was a gift from Noboru Mizushima (Addgene plasmid 38249)⁵². The 37 C-terminal amino acids of Omp25 (also known as Synj2bp) localize GFP to the OMM (GFP–OMM)⁵³. The donor vector was created by obtaining the GFP–OMM coding sequence via NotI digestion and inserting it via blunt-end cloning into the expression vector pEx-CAG-stop-bpA, which was digested with BglI.

Animals. *MitoTag* knock-in mice were generated by recombinase-mediated cassette exchange into the *Rosa26* locus of mouse embryonic stem cells as described previously^{54,55}. In brief, the donor vector flanked by a pair of phiC31 integrase attB recognition sites was co-electroporated with C31-integrase expression vector into IDG 3.2 embryonic stem cells that harbor a pair of phiC31 integrase attP sites within one allele of the acceptor locus. By phiC31-mediated recombination of attB and attP sites, a single copy of the GFP–OMM cassette was integrated into the *Rosa26* locus. A neomycin resistance gene located upstream of the cytomegalovirus early enhancer–chicken β -actin promoter enables the selection of recombinant embryonic stem cells. These were first selected with G418 (140 μ g ml⁻¹) for 1 week; then resistant colonies were isolated and analyzed for correct cassette exchange by Southern blot analysis as described previously^{54,56}. Screened cells were injected into C57BL/6 blastocysts. The obtained chimeras were identified by PCR using the primers (5'–3') GTTGTGCCAGTCATAGCCGAATAG-3 and CACGCTTCAAAGCGCAGCTCTG (PCR product 280 base pairs (bp)), and further bred to C57BL/6 mice. Genotyping of *MitoTag* mice was performed with the following primers (5'–3'), which distinguish homozygous (PCR product 604 bp) and heterozygous (PCR product 604 and 324 bp) mice: GCACCTTGCTCTCCCAAAGTC, CATAGTCTAACTCGCGACTG, AGATCCGCCACAACATCG and TCTCAGGAAGCCCAAAC. The *MitoTag* mouse line is available from The Jackson Laboratory as JAX#032675 (*Rosa26*–CAG–LSL–GFP–OMM).

Thy1:mito-RFP mice⁵⁷ were used to measure mitochondrial transport and shape in ChAT:Cre/GFP–OMM crossings (Supplementary Fig. 2a,b). In these transgenic mice, tagRFP is localized to the mitochondrial matrix and expressed in many neurons via the Thy1 promoter. In addition, tissue was used for expansion microscopy (matrix label; Fig. 1d) and to evaluate the immunocapture protocol via 'spike-in' experiments (Fig. 2 and Supplementary Fig. 5a–c).

To express GFP–OMM in different cell types, we used the following Cre-driver lines: Emx1:Cre (neural cells in the forebrain; #005628; The Jackson Laboratory)⁵⁸; ChAT:Cre (cholinergic neurons; #006410B6; The Jackson Laboratory)⁵⁹; L7:Cre (PC; #004146; The Jackson Laboratory)⁶⁰; Gabra6:Cre (cerebellar GC; gift of U. Fünfschilling and K.A. Nave, MPI Goettingen)⁶¹; Gfap:Cre (astrocytes; #024098; The Jackson Laboratory)⁶² and Rbp4:Cre (principle neurons layer 5/6; 031125-UCD; Mutant Mouse Resource and Research Center (MMRRC))^{63,64}.

To probe mitochondrial morphology in disease models, we used transgenic APPS1 (ref. 65) and SOD1^{G93A} (#004435; The Jackson Laboratory)⁶⁶ mice, with the age of 9 months and the age range of 2–5 months, respectively. Transgenic APPS1 mice express mutant amyloid precursor protein KM670/671NL (Swedish) and mutant Presenilin 1 G384A from humans driven by the Thy1 promoter.

The Mcu knockout-first allele mouse strain was obtained from MMRRC (C57BL/6N–Mcutm1a(EUCOMM)Hmgu/H). To generate the conditional Mcu^{FL/FL} mouse line, we bred Mcu^{tm1a} mice with ACTB-FLPe mice (FLP-Deleter: #019100; The Jackson Laboratory)⁶⁷ and tested cassette removal via PCR. Mice were further bred with Gabra6:Cre mice to obtain GC-specific Mcu knockout animals. Mice were genotyped by PCR using the following primer (5'–3'): TGGGTGTTGATTACAAAGTTTCA, GGTGTGCTCTGACCTCCAC and GAACTTCGGAATAGGAACCTTCG (PCR product 300 bp for wild-type, 462/118 bp for mutant allele). Disruption of the endogenous locus was confirmed by western blot analysis and immunofluorescence staining (Fig. 6f,g). Although no homozygous Mcu^{tm1a} mice were born, the GC-specific deletion of Mcu did not cause obvious behavioral phenotype up to 6 months of age.

The Rmdn3 knockout-first allele mouse strain was created from embryonic stem cell clone EPD0131_4_D01, obtained from the KOMP Repository (<https://www.komp.org>) and generated by the Wellcome Trust Sanger Institute⁶⁸. Targeting vectors used were generated by the Wellcome Trust Sanger Institute and the Children's Hospital Oakland Research Institute as part of the Knockout Mouse Project (3U01HG004080). Mice were genotyped by PCR using the following primer (5'–3'): GCCTCAGCAGCGAGTACTTTTAC, GGTCATGTAACTCCAGCCGCTCTGG and GGGATCTCATGCTGGAGTCTTTCG (PCR product 231 bp for wild-type and 546 bp for mutant allele). Disruption of the endogenous locus was confirmed by western blot analysis and immunofluorescence staining (Fig. 7c,d). Loss of Rmdn3 caused no obvious behavioral phenotype up to 3 months of age.

All animal experiments were approved by the responsible regulatory agencies (Regierung von Oberbayern). If not mentioned otherwise, male and female animals of the species *Mus musculus*–C57BL/6 (mixed N/J) background were used within the age range of 6 weeks to 6 months.

Neonatal virus injection to deliver Cre. To excise the stop-cassette in *MitoTag* mice via adeno-associated viral delivery of Cre, we performed neonatal injections

as described by Brill et al.⁶⁹. A volume of 3 μ l AAV9-hSyn-iCre (codon-improved Cre under the human synapsin promoter; titer: 8.494e13 ml⁻¹; Penn Vector Core) was injected to achieve GFP–OMM expression in neurons (Supplementary Fig. 1f).

Imaging of axonal transport and neuromuscular health assessment. To assess mitochondrial transport and shape, we crossed ChAT:Cre/GFP–OMM mice to Thy1:mito-RFP mice and compared Cre⁺ and Cre⁻ littermates. Evaluation of transport and shape was exclusively based on mito-RFP and GFP–OMM and used to confirm genotype.

Triangularis sterni explants were isolated from adult mice as previously described^{65,70}. In brief, the rib cage was explanted postmortem (including the triangularis sterni muscle and its innervating intercostal nerves) and transferred into a dish with oxygenated Ringer's solution containing (in mM): 125 NaCl, 2.5 KCl, 1.25 NaH₂PO₄, 26 NaHCO₃, 2 CaCl₂, 1 MgCl₂ and 20 glucose. Extraneous tissues were removed, and the explant was pinned into a Sylgard-coated 35 mm dish using insect pins, super-fused with warm oxygenated Ringer's solution and kept heated at 33–35 °C during the whole imaging session. Mitochondrial transport in the intercostal nerves was assessed using an Olympus BX51WI epifluorescence microscope equipped with $\times 20/0.5$ numerical aperture (N.A.) and $\times 100/1.0$ N.A. water immersion objectives, an automated filter wheel (Sutter) and a cooled CCD camera (Retiga EXi; Qimaging), controlled by μ Manager (v1.48; <https://micro-manager.org>). Neutral density filters were used to minimize phototoxicity and bleaching.

To assess neuromuscular synapse structure, we fixed triangularis sterni muscles on ice for 1 h in 4% paraformaldehyde (PFA)/PBS and stained them overnight at 4 °C with α -bungarotoxin/biotin-XX conjugate (50 μ g μ l⁻¹ diluted 1:50 in PBS; Invitrogen) to visualize acetylcholine receptors and Alexa Fluor 647-conjugated phalloidin (200 U ml⁻¹ methanol, diluted 1:50 in PBS; Invitrogen) to visualize muscle fibers. The sample was subsequently incubated in a streptavidin–Alexa Fluor 405 conjugate (Invitrogen) for 1 h at room temperature. The area of neuromuscular junctions was determined using ImageJ/Fiji software⁷¹ by thresholding ('Otsu' algorithm) the α -bungarotoxin staining. Intensity was determined within the thresholded area with background subtraction.

Mitochondrial isolation and immunocapture protocol. Mitochondria were isolated from freshly collected mouse tissue as described by Wettmarshausen and Perocchi⁷². In brief, mice were anesthetized with a lethal dose of isoflurane and transcardially perfused with heparin (19.5 U ml⁻¹; Sigma) in PBS. The tissue of interest was dissected, weighted and minced with a Dounce glass homogenizer using three complete up-and-down cycles of an A-type pestle in isolation buffer containing (in mM): 220 mannitol, 80 sucrose, 10 HEPES and 1 EDTA, pH 7.40, and supplemented with 1% essentially fatty acid-free BSA (A7030; Sigma). During all steps, the sample was kept on ice or at 4 °C. Next, the cells were opened by nitrogen cavitation using a cell disruption vessel (model 4635–39; Parr Instrument Company) at 800 psi and under stirring at 60 r.p.m. for 10 min. Upon release from the disruption vessel, 1 \times protease inhibitor (cComplete, EDTA-free Protease Inhibitor Cocktail; Roche) was added to the resulting total tissue fraction, and nuclei and debris were removed by centrifugation for 10 min at 600g. The supernatant was transferred and centrifuged again. The resulting postnuclear tissue fraction was filtered through a preperparation filter (#130-041-407; Miltenyi Biotec).

From this fraction, a volume equivalent to 20 mg initial tissue was centrifuged for 3 min at 12,000g, and the pellet was washed twice with isolation buffer without BSA to obtain the crude mitochondrial fraction (CMF). For respiratory measurements, the final CMF was gently resuspended in 30 μ l of isolation buffer with 0.2% essentially fatty acid-free BSA. For western blot analysis, the pellet was immediately stored at –20 °C.

For immunocapture against Tom22 (refs. 15,73) or GFP–OMM, the postnuclear tissue fraction was diluted to a concentration of maximal 2 mg tissue ml⁻¹ in immunocapture buffer (ICB) containing (in mM): 137 KCl, 2.5 MgCl₂, 3 KH₂PO₄, 10 HEPES, 1 EDTA, pH 7.40, and supplemented with 1% essentially fatty acid-free BSA and 0.5 \times protease inhibitor. Fifty-microliter microbeads coated with mouse IgG, antibodies against Tom22 (#130-096-946; Miltenyi Biotec), GFP (#130-091-125; Miltenyi Biotec) or CD4 (#130-047-102; Miltenyi Biotec) were added and incubated on a shaker (60 r.p.m.) for 30–90 min at 4 °C. Incubation was dependent on cell type abundance within tissue and adjusted accordingly, for example for cortex from Emx:Cre/GFP–OMM 30 min and for cortex from ChAT:Cre/GFP–OMM 90 min. To separate microbead-coated mitochondria from the solution, we placed LS columns (#130-042-401; Miltenyi Biotec) in a magnetic QuadroMACS Separator (#130-090-976; Miltenyi Biotec) and equilibrated with 3 ml of ICB. The immunocapture was applied to the column in 3-ml steps, followed by three 3-ml washing steps with ICB. The column was removed from the separator, and mitochondria were gently flushed out in 4 ml of ICB with a plunger. Mitochondria were pelleted by centrifugation for 3 min at 12,000g and washed twice with isolation buffer without BSA. For respiratory measurements, the final pellet was gently resuspended in 30 μ l of isolation buffer with 0.2% essentially fatty acid-free BSA. For western blot analysis, the sample was immediately stored at –20 °C.

We deliberately avoided use of an additional Percoll gradient for further purification⁷⁴ to preserve organelle interactions and mitochondrial integrity⁷⁵. This results in some level of commonly known contaminations (Supplementary Fig. 3a,d), which, however, is largely eliminated by normalization to IC Tom, where

it is equally present. However, if purity is desired over organelle viability, yield and time, purity can be improved by a Percoll gradient after immunocapture.

Protein amount determination. Protein concentration in samples was determined using the BCA assay (Pierce BCA Protein Assay Kit; Thermo Fisher Scientific) according to the manufacturer's instructions and using BSA as the standard. Sample buffer was used to correct for measurement alterations caused by detergent or BSA.

Measurement of mitochondrial respiration. The oxygen consumption rate (OCR) of mitochondria during respiration was measured in the assay solution MAS-1X containing (in mM): 70 sucrose, 220 mannitol, 10 KH_2PO_4 , 5 MgCl_2 , 2 HEPES, 1 EGTA and 0.2% essentially fatty acid-free BSA, using a Seahorse XFe96 Extracellular Flux Analyzer (Seahorse Bioscience). A specific amount of CMF or immunocaptured mitochondria was added in a volume of 10 μl to each well in a 96-well plate (see below for substrate details). To attach mitochondria, we centrifuged the plate at 2,000g, 4°C for 20 min. Substrate mixture was added, and the plate was brought to equilibrium at 37°C. Respiration was determined in the presence of either succinate/rotenone (10 mM/2 μM), pyruvate/malate (10 mM/2 mM) or palmitoyl-carnitine/malate (50 μM /2 mM)^{76,77} as substrates. First, basal measurements of OCR (state 2) were obtained. Next, adenosine diphosphate (ADP; 4 mM) was injected (state 3), followed by sequential injections of oligomycin (1.5 μM ; state 4a), carbonyl cyanide *m*-chlorophenyl hydrazone (CCCP; see later concentration per substrate; state 3u) and antimycin A/rotenone (4 μM /2 μM) to disrupt mitochondrial respiration. Together, this injection series allowed for determination of ADP-uncoupled respiration (ADP), proton leak (oligomycin), maximal respiration (CCCP) and nonmitochondrial residual oxygen consumption (antimycin A/rotenone). Samples from individual isolations were run in at least eight technical replicates using typical mixing (1 min) and measurement cycle times (3 min). For each injection, technical replicates were counted only when there was a response to the injection and mitochondria did not detach during the experiment. Each state was corrected for the nonmitochondrial residual oxygen consumption value obtained with antimycin A/rotenone injection.

The following amounts of mitochondria and CCCP concentrations were used, respectively, for the indicated substrates: (1) cortical mitochondria obtained by differential centrifugation (CMF) of 2 μg and 10 μM for succinate/rotenone and pyruvate/malate; (2) cortical mitochondria obtained by immunocapture (IC) of 1 μg and 10 μM for succinate/rotenone and 2 μg and 10 μM for pyruvate/malate; and (3) cerebellar mitochondria obtained by IC of 2 μg and 7.5 μM for succinate/rotenone, 3 μg and 7.5 μM for pyruvate/malate and 8 μg and 3 μM for palmitoyl-carnitine/malate.

Coupling efficiency (CE) was calculated as the ATP-linked OCR ((basal-oligomycin)/basal respiration); respiratory control ratios (RCR) were calculated as the (ADP-linked/oligomycin OCR) readings and the spare capacity ratio (SCR) as the maximal respiration (CCCP driven/basal). Analysis was performed with Seahorse XFe96 Wave software (v.2.3.0.19; Agilent), Microsoft Excel 2016 and GraphPad Prism v.7 (GraphPad Software).

Mitochondrial calcium uptake. Calcium uptake of immunocaptured mitochondria was performed as described by Wettmarshausen and Perocchi⁷² with the following modifications: mitochondria (50 μg) were resuspended in respiration buffer containing (in mM): 137 KCl, 2.5 MgCl_2 , 3 KH_2PO_4 , 10 HEPES, 5 succinate, 5 malate, 5 glutamate, 0.2% essentially fatty acid-free BSA, pH 7.4, supplemented with 100 nM CalciumGreen-5N (C3737; Thermo Fisher Scientific) in the absence or presence of 10 μM Ru360 (#557440; Sigma). Fluorescence (excitation 485/emission 530) was measured via a microplate reader (CLARIOstar; BMG Labtech) in 2-s intervals for a total of 24 min with the injection of 20 μM CaCl_2 in the assay buffer every 3 min at 25°C.

Calcium uptake capacity was calculated as the differential area under the curve (ΔAUC) between the presence and absence of Mcu inhibitor Ru360. In brief, the first CaCl_2 injection was ignored because of residual EDTA from the immunocapture buffer. Traces were background corrected and normalized to the injection time point, and AUC was calculated. Finally, the difference between $\text{AUC}_{-\text{Ru360}}$ and $\text{AUC}_{+\text{Ru360}}$ per sample is shown as percentage of $\text{AUC}_{+\text{Ru360}}$. Animals within the age range of 8 weeks to 4 months were used from either C57BL/6 mix J, N background or the floxed Mcu strain (Fig. 6e,i).

Western blot. For western blot analysis, material was first lysed in RIPA buffer containing (in mM): 50 Tris-HCl, pH 8.0, 150 NaCl, 0.1 EDTA and 1% Triton X-100, 0.25% Nonidet P-40, 0.1% SDS, as well as protease inhibitor (cOmplete, EDTA-free Protease Inhibitor Cocktail; Roche) on ice for 30 min with frequent vortexing. Protein concentration was determined via BCA assay; samples were mixed with 1 \times LDS sample buffer (#NP0007; Thermo Fisher Scientific) containing 50 mM dithiothreitol (DTT) and boiled at 70°C for 10 min. Per sample, 10 μg of protein was used in the case of mitochondrial isolations and whole-tissue comparison; 20 μg was used in the case of total cerebellar lysates to evaluate Rmdn3 expression (Fig. 7c). Using SDS polyacrylamide gels (12% or 4–20%), we separated samples via electrophoresis with Tris-glycine buffer (25 mM Tris base, 192 mM glycine, 0.1% SDS) and transferred on PVDF membrane (0.2 μm ; Millipore) with Twobin buffer containing 25 mM Tris base, 192 mM glycine and

20% methanol using the TurboBlot semidry system (Bio-Rad) with the following settings: 20 V maximum, 1.3 A, 12 min. After transfer, membranes were washed with water and air-dried, followed by SyproRuby staining (#S11791; Thermo Fisher Scientific) for total protein quantification according to the manufacturer's instructions. SyproRuby signals were acquired using UV light on the Fusion FX7 machine (Vilber Lourmat). To remove total protein staining, we incubated membranes in 3% skim milk/TBST (0.1% Tween 20 in TBS) for 30 min at room temperature and blocked them for a further 30 min in new solution. Incubation with primary antibody was performed overnight on a shaker (60 r.p.m.) at 4°C in 3% skim milk/TBST using the following antibodies: mouse Actin (A2228, Sigma; 1:4000), Ak4 (sc271161; 1:100; Santa Cruz), ATP5a (ab14748; 1:10,000; Abcam), CypD (ab110324; 1:5,000; Abcam), GFP (sc-9996; 1:500; Santa Cruz); and rabbit Calreticulin (12238; 1:1,000; Cell Signaling), Cox4i1 (AP22111a; 1:1,000; Abgent), Emre (sc-86337; 1:500; Santa Cruz), Gldc (HPA002318; 1:1,000; Sigma), Got2 (ab171739; 1:1,000; Abcam), Lamin B1 (ab16048; 1:1,000; Abcam), Mcu (HPA016480; 1:1,000; Sigma), Ociad2 (HPA040979; 1:1,000; Sigma), Rmdn3 (ab189845; 1:2,000; Abcam), Sfxn5 (ab172971, Abcam; 1:2,000), SNAP25 (5308; 1:2,000; Cell Signaling), Tomm20 (ab78547; 1:1,000; Abcam) and RFP (AB234, Evrogen; 1:5,000). Membranes were washed three times in TBST at room temperature on a shaker (60 r.p.m.) for 10 min, followed by a 2-h incubation of either goat anti-mouse horseradish peroxidase (HRP) or goat anti-rabbit HRP (1:5,000; Bio-Rad) in 3% skim milk/TBST on a shaker (60 r.p.m.) at room temperature. After washing, membranes were incubated with ECL Prime (RPN2232; GE Healthcare Life Sciences) according to the manufacturer's instructions, and signals were acquired using the Fusion FX7 machine. A second round of antibody probing was performed for antibodies from a different species. After extensive washing in TBST at room temperature, membranes were blocked again and incubated overnight with primary antibody. Cross-reactivity of antibodies from rabbit and mouse was excluded in prior experiments.

For quantification, samples were run as technical triplicates on one membrane, and the mean was further used for graphs and statistics, with the exception of Supplementary Fig. 5b, where sample amounts limited the analysis to one per experiment, and Fig. 6c,f, where samples were run as duplicates. Nonsaturated images were used and analyzed with Image Studio Lite software (LI-COR) and Microsoft Excel 2016. Signals per lane were background subtracted and normalized with total protein signals (SyproRuby) using dosimetry; results were expressed as FC to a given sample on the membrane. Mitochondrial content (evaluated by ATP5a, CypD and Tomm20) was further used for normalization when proteins were compared between different isolations. Uncropped western blots for all depicted blots in figures are shown in Supplementary Fig. 18.

Sample preparation for mass spectrometry. Samples for mass spectrometry were obtained from 8- to 9-week-old male mice. Mitochondria were immunocaptured from the cerebellum according to the described protocol with the alteration that the final mitochondrial pellet was washed twice in isolation buffer without EDTA and BSA. Samples were lysed in 100 μl SDT lysis buffer (4% w/v SDS, 100 mM DTT, 100 mM Tris-HCl, pH 7.6) by heating for 5 min at 95°C and ultrasonication (Vialtweeter: six times for 30 s, 100% amplitude, 50% cycle, maximum power; Hielscher Ultrasonics). Debris and nondissolved material were removed by centrifugation for 10 min at 20,000g. Protein concentrations were estimated using the Pierce 660-nm assay supplemented with the ionic detergent compatibility reagent (Thermo Fisher Scientific) with a dilution series of bovine albumin in SDT buffer for calibration. An amount of 15 μg was subjected to protein digestion using the filter-aided sample preparation⁷⁸ with small modifications. In brief, 30 kDa Vivacon filters (Sartorius) were used. The alkylation step was followed by incubation with 50 U Benzonase (Sigma-Aldrich) in 50 mM Tris-HCl, pH 8 and 1 mM MgCl_2 . Afterward, three washing steps with 100 μl 8 M urea in 100 mM Tris-HCl, pH 8, were implemented. Proteins were digested for 16 h with 0.3 μg LysC (Promega) followed by 4-h incubation with 0.15 μg trypsin (Promega). Peptides were eluted into collection tubes and desalted using C18 stop-and-go extraction⁷⁹. Samples were dried after elution by vacuum centrifugation.

Whole cerebellum samples were lysed in a modified RIPA buffer (1% Triton X-100, 0.5% sodium deoxycholate, 0.1% SDS, 150 mM NaCl, 5 mM EDTA, 50 mM Tris-HCl, pH 8). Cell debris and undissolved material were removed by centrifugation for 10 min, at 16,000g, 4°C. A protein amount of 20 μg was further diluted 1:2 with water, and MgCl_2 (10 mM) was added. Afterward, 25 U Benzonase (Sigma-Aldrich) was added, and the DNA digestion was performed for 30 min at 37°C. Protein digestion was performed using filter-aided sample preparation as described earlier without addition of Benzonase.

Liquid chromatography–tandem mass spectrometry data acquisition. Samples were analyzed on an Easy nLC-1000 nano UHPLC (Thermo Fisher Scientific) coupled online via a Nanospray Flex electrospray ion source (Thermo Fisher Scientific) equipped with a column oven (Sonation) to either a Q-Exactive or a Q-Exactive HF mass spectrometer (Thermo Fisher Scientific). An amount of 1.3 μg peptides was separated on self-packed C18 columns (300 mm \times 75 μm , ReproSil-Pur 120 C18-AQ, 1.9 μm ; Dr. Maisch) using a binary gradient of water (A) and acetonitrile (B) supplemented with 0.1% fatty acid (0 min, 2% B; 5 min, 5% B; 185 min, 25% B; 230 min, 35% B; 250 min, 60% B).

The dataset from PC was analyzed on a Q-Exactive MS. Full mass spectrometry spectra were acquired at a resolution of 70,000 (automatic gain control (AGC) target: $3E+6$). The ten most intense peptide ions were chosen for fragmentation by higher-energy collisional dissociation (resolution: 17,500, isolation width: $2m/z$, AGC target: $1E+5$, normalized collision energy (NCE): 25%). A dynamic exclusion of 120 s was applied for fragment ion spectra acquisition. The datasets from the cerebellum, GC and astrocytes (A) were analyzed on a Q-Exactive HF MS with slightly adjusted settings. For full mass spectrometry spectra, a resolution of 120,000 was applied. The 15 most intense ions were chosen for fragmentation (resolution: 15,000, isolation width: $1.6m/z$, AGC target: $1E+5$, NCE: 26%).

Liquid chromatography–tandem mass spectrometry data analysis. Peptide identification, label-free quantification (LFQ) and iBAQ of proteins were performed with MaxQuant for each dataset separately (v.1.5.4.1 for the PC dataset; 1.5.5.1 for the dataset from cerebellum, GC and astrocytes) using default settings⁸⁰. In brief, a canonical database of the reviewed reference mouse proteome (UniProt, download: 8 June 2016; 16,798 entries) was used for database search. The astrocyte dataset from the cerebellum was analyzed together with data from astrocytic mitochondria from the cortex because both datasets (cerebellum and cortex) were generated in parallel from the same biological replicate. Because increased sample numbers increase the number of peptide identifications, this part was done together; however, all further data analysis steps were exclusively performed on cerebellar mitochondria. The false discovery rate (FDR) for both peptides and proteins was adjusted to less than 1% using a target and decoy approach (concatenated forward/reverse database). The ‘match between runs’ option was enabled using a time window of 2 min. LFQ required at least two ratio counts of unique peptides. The mass spectrometry proteomics data have been deposited to the ProteomeXchange Consortium via the PRIDE (ref. ⁸¹) partner repository with the dataset identifier: mitochondria from PC (PXD010772), from GC (PXD010774) and from astrocytes (PXD010781); and whole cerebellum (PXD013380).

Protein intensities were further analyzed in Perseus (v.1.6.1.1.)^{82,83}. The bioinformatics analysis is depicted in Supplementary Fig. 6. First, protein identifications (IDs) from the three mass spectrometry experiments were merged against the reviewed reference mouse proteome including annotation from *MitoCarta*¹⁸ and LocTree3 (ref. ⁸⁴) for subcellular localization. Only proteins with at least two unique peptides were further considered for relative quantification. Protein LFQ intensities were \log_2 transformed. Second, for relative quantification, the protein \log_2 LFQ ratios were calculated by subtracting the \log_2 value of IC Tom from IC GFP separately for each biological replicate. Next, proteins that were relatively quantified in less than three biological replicates were removed, leading to a group of 3,130 proteins that were consistently quantified in all three datasets from PC, GC and astrocytes (background list for over-representation analysis in WebGestalt⁸⁵). Finally, the \log_2 FC of each protein between cell types (comparisons: PC/GC, PC/astrocyte (PC/A) and GC/astrocyte (GC/A)) was analyzed by a two-sided *t*-test (with ≥ 3 biological replicates, randomizations: 500, permutation-based FDR = 0.05). Proteins with \log_2 FC values that passed the permutation-based FDR criterion are marked as dark gray circles in Fig. 3c and Supplementary Fig. 7a–c. The scatterplot summarizing changes in PC/A versus GC/A is depicted in Fig. 3c and Supplementary Fig. 7d, which show the \log_2 FC of PC/A (*x* axis) and GC/A (*y* axis) for each protein that passed the FDR criterion in at least one of the two comparisons.

From the pairwise *t*-tests between cell types (Supplementary Fig. 7a–c), proteins were considered to be changed if their \log_2 FC was $\geq |1|$. Thus, they were further analyzed for their enrichment in a specific cell type by using the online Venn diagram tool (<http://bioinformatics.psb.ugent.be/webtools/Venn/>). Here, 18, 51 and 114 proteins were identified to be enriched in PC, GC and astrocytes, respectively (Fig. 3b and Supplementary Fig. 7d) using the following definitions for cell type specificity: ‘PC enriched’ with FC > 1 in PC/A, combination A (FC > 1 in PC/A and PC/GC) and combination B (FC > 1 in PC/GC only); ‘GC enriched’ with FC > 1 in GC/A, combination A (FC < –1 in PC/A and PC/GC, FC > 1 in GC/A), combination B (FC > 1 in GC/A, FC < –1 in PC/GC) and combination C (FC < –1 in PC/GC only); and ‘A enriched’ with FC < –1 in PC/A and/or GC/A. These groups are color-coded in the scatterplot in Supplementary Fig. 7d comparing PC/A versus GC/A.

For over-representation analysis (ORA) on KEGG pathways (Supplementary Fig. 7e) and the biological process category of gene ontology processes (GO Term; Supplementary Fig. 7f), a WEB-based Gene Set Analysis Toolkit (WebGestalt)⁸⁵ was used with the following datasets: proteins found in ≥ 3 biological replicates among all experiments ($n = 3,130$) as background against the candidates enriched in astrocytes ($n = 114$) and merged candidates found in neurons (GC enriched, PC enriched, shared; $n = 74$). Standard parameters for the enrichment analysis were used with the following settings: minimum number of Entrez Gene IDs in the category: 5; maximum number of Entrez Gene IDs in the category: 2000; FDR method: Benjamini–Hochberg (multiple test adjustment); and significance level: top 10.

To further validate enriched KEGG pathways, we used the list of shared proteins among the three cell types ($n \geq 3$ replicates). Before filtering through the online tool ‘Kegg mapper’ (<https://www.genome.jp/kegg/mapper.html>)⁸⁶,

the average \log_2 FC (IC GFP/ IC Tom) values per biological replicates were calculated per cell type. The heat map in Fig. 5a was generated based on the KEGG pathway, mmu01212, and was further curated against the following criteria: strict involvement in beta-oxidation, annotation in *MitoCarta*¹⁸ and mitochondrial localization in the UniProt database (March 2017).

Enrichment of mitochondrial protein abundance was calculated based on iBAQ values⁸⁷. First, the average \log_{10} iBAQ value per protein per group of biological replicates was calculated for immunocaptures. Second, the average was calculated over all proteins annotated as mitochondrial (magenta) and nonmitochondrial (gray) based on *MitoCarta*¹⁸ and LocTree3 (ref. ⁸⁴) annotations (see Supplementary Fig. 3c). Finally, the difference between these two groups was transformed to FC (linear). Similar calculations were performed on the proteomics datasets from whole cerebellum and the reference dataset of Percoll-purified mitochondria from Pagliarini et al.⁷

To compare the immunocapture approach with recent studies, we generated Venn diagrams with the online Venn diagram tool (<http://bioinformatics.psb.ugent.be/webtools/Venn/>) comparing IC Tom from cerebellum with the proteomics dataset from cerebellar mitochondria published by Pagliarini et al.⁷, from whole cerebellum published by Sharma et al.¹⁷ and from *MitoCarta* (Supplementary Fig. 3b). For this comparison, proteins found in ≥ 9 samples of IC Tom were considered.

Histology and immunofluorescence staining. Animals were killed with isoflurane and transcardially perfused first with heparin (19.5 U ml^{-1} ; Sigma) in PBS followed by 4% PFA in PBS. Tissues were kept in 4% PFA/PBS overnight at 4°C and subsequently cut using a vibratome (Leica).

If not mentioned differently, all staining steps were performed on a shaker (60 r.p.m.) at room temperature. Depending on the epitope, tissue sections were permeabilized with different conditions (see Supplementary Table 1), extensively washed, and blocked using 2% fish gelatin (Sigma), 2% FBS (Thermo Fisher Scientific) and 2% BSA (A7030; Sigma) in PBS for 1 h. For primary antibodies produced in mouse, sections were incubated with mouse Fab fragments (1:100 in PBS; Bio-Rad) for 1 h. Incubation with primary antibody was performed in 10% blocking/PBS solution at 4°C overnight (see Supplementary Table 1). After extensive washing, secondary antibodies (1:1,000) were applied in 10% blocking/PBS for 2 h. Tissue sections were further stained with Hoechst (Hoechst 33342; 0.01 mg ml^{-1} in PBS; Molecular Probes) for 10 min and mounted using Vectashield mounting medium (H-1000; Vector Laboratories).

To perform double labeling of mitochondrial markers with antibodies raised in the same species, we used the Zenon Alexa Fluor 647 Rabbit IgG Labeling Kit (Z25308; Thermo Fisher Scientific) according to the manufacturer’s instructions. In brief, $1 \mu\text{g}$ of rabbit anti-Sfxn5 antibody (ab172971; Abcam) was linked to $10 \mu\text{l}$ of component A and after 5-min incubation stopped with $10 \mu\text{l}$ of component B. After incubation with secondary antibody and extensive washing, sections were incubated with Zenon complex and Hoechst for 2 h. The sections were washed three times in PBS for 5 min. Importantly, to stabilize staining for longer storage, we further incubated sections in acryloyl-X, SE, 6-(acryloyl)amino)hexanoic acid, succinimidyl ester (AcX; 1:100 in PBS; A20770; Thermo Fisher Scientific) for 4 h at 4°C and mounted them using Vectashield mounting medium (H-1000; Vector Laboratories).

To visualize amyloid plaques and amyloid- β deposition in APPPS1 mice, we used Hoechst (Hoechst 33342; 0.01 mg ml^{-1} in PBS; Molecular Probes), which superiorly detected the entire plaque with its periphery, a feature that was reported for Alzheimer’s disease mouse models by Uchida and Takahashi⁸⁸. We further confirmed amyloid- β detection using the antibody clones 4G8 (#800708; BioLegend) and 6E10 conjugated to Alexa Fluor 647 (#803020; BioLegend), which, however, penetrated less well in our staining conditions. For human tissue, the amyloid- β antibody clone 6F/3D (M0872; Dako) was used.

For human tissue sections the following changes for immunohistochemical stainings were applied (see Supplementary Table 2): after deparaffination, heat-induced antigen retrieval was performed on PFA fixed tissue. After 10% FCS/PBS unspecific binding blockade, sections were incubated with primary antibodies in Dako Diluent (#52022; Dako) at 4°C overnight. After extensive washing with Wash Buffer (#53006; Dako) and autofluorescence removal treatment (#2160; Merck), secondary antibodies and 4,6-diamidino-2-phenylindole (DAPI; nuclear counterstain, 1:2,000) were diluted in PBS and incubated at room temperature for 1 h. Slides were coverslipped with Fluoromount Mounting Medium (Sigma). For sections that require tyramide signal amplification, endogenous peroxidase blockade (S2023; Dako) was performed before addition of 10% FCS/PBS. After incubation with primary antibodies, slides were incubated at room temperature for 30 min with anti-rabbit HRP, followed by incubation with tyramide signal amplification (FP1170; Perkin Elmer) for 10 min at room temperature as a secondary system. Autofluorescence removal treatment was performed before DAPI staining. Use of human samples was in accordance with institutional ethical guidelines and approved by the ethics committee of the University of Geneva (Switzerland). Written informed consent to use autopsy samples for research purposes was obtained for all samples with exceptions for autopsies that were performed more than 20 years ago. In all cases, no samples were used from patients who refused involvement in research projects. Patient information is provided in

Supplementary Table 3. Data from human cerebellum are representative of one experiment; data from the human cortex and spinal cord are representative of one experiment performed on at least three different cases.

Fluorescence cytometry. The crude mitochondrial fraction from 20 mg cortex samples was resuspended in 100 μ l of 4% PFA/PBS and incubated in the dark for 5 min at room temperature. Samples were washed three times with PBS and resuspended in 100 μ l. Twenty microliters of fixed mitochondria was used per staining. First, the sample was washed once with 0.5% BSA/PBS and then incubated with APC-conjugated antibodies: IgG₁ or Tom22 (1:25; Miltenyi Biotec) in the dark, 4 °C, 60 r.p.m. for 60 min. Samples were washed three times with 0.5% BSA/PBS and finally resuspended in 100 μ l PBS. For flow cytometry, the sample was diluted 1:20 with PBS and analyzed using a CyAn ADP 9 flow cytometer (equipped with 405-, 488- and 642-nm lasers; Beckman Coulter). The flow rate was adjusted accordingly, and optical parameters (forward scatter (FSC) and sideward scatter (SSC)) were scaled logarithmically to allow for optimal identification and separation of small particles. Based on light-scattering properties (FSC-log versus SSC-log), 100,000 mitochondria were acquired per sample. Using FlowJo software (v.10; Tree Star), mitochondria were gated by FSC and SSC, as well as pulse width to discriminate doublets. Then Tom22-APC staining (APC, 665/20) intensities were manually gated against IgG₁-APC control samples to define mitochondria. From this, individual gates for GFP-OMM (FITC, 530/40) and mito-RFP (PE, 575/25) were gated according to the Cre⁻ mitochondria. In Supplementary Fig. 4b, values from ≥ 4 biological replicates are shown as mean \pm s.e.m., as well as the histogram of the samples closest to mean with IgG₁ control (gray histogram).

Confocal microscopy. Tissue sections were scanned either on an upright FV1000 confocal microscopy system (Olympus) equipped with $\times 4/0.28$ N.A. air, $\times 10/0.4$ N.A. air, $\times 20/0.85$ N.A. oil, $\times 40/1.35$ N.A. oil and $\times 60/1.42$ N.A. oil immersion objectives or an inverted FV3000 confocal microscopy system (Olympus) equipped with $\times 4/0.16$ N.A. air, $\times 20/0.75$ N.A. air and $\times 40/0.95$ N.A. air objectives. Images were acquired using standard filter sets, and intensity projections were generated using the open source software ImageJ/Fiji⁷¹ and Adobe Photoshop.

Image processing and representation. For figure representation, different channels of confocal image series were combined in pseudocolor using the 'screen' function in Adobe Photoshop. Contrast and brightness were equally adjusted across the entire image. In Supplementary Fig. 9, immunofluorescence stainings on Cre⁻ tissue and control (omission of primary antibody) were acquired with the same settings and were adjusted with the same processing parameters. In nonquantitative panels, gamma was adjusted nonlinearly to enhance visibility of low-intensity objects. Figures were assembled in Adobe Illustrator.

Protein retention expansion microscopy. Expansion microscopy on mouse cortical tissue sections was performed as previously described⁸⁹. In brief, the cerebrum of Emx1:Cre/GFP-OMMxThy1:mito-RFP mice was fixed using 4% PFA/PBS and sectioned in 100 μ m thick sagittal section using a vibratome (Leica). To enhance GFP-OMM signals, we stained sections against GFP as described previously using 0.2% Triton X-100/PBS for permeabilization. Next, samples were cross-linked with acryloyl-X (AcX; 1:100 in PBS; A20770; Thermo Fisher Scientific) at 4 °C for 6 h, gelled with freshly prepared monomer solution (containing in g per 100 ml: 8.6 sodium acrylate, 2.5 acrylamide, 0.15 N,N'-methylenebisacrylamide and 11.7 sodium chloride in PBS) and digested with Proteinase K (8 U ml⁻¹) at 37 °C overnight. For expansion, samples were first incubated in PBS and then in distilled water. An expansion factor of ~ 2 - to 3-fold was estimated from the sample. Data are representative of $n=2$ independent experiments.

Electron microscopy. Mitochondria (as crude mitochondrial fraction or immunocapture) were incubated in fixative containing 2.5% glutaraldehyde, 4% PFA, 0.1 M sodium cacodylate buffer, pH 7.2 for 10 min before being centrifuged and, after supernatant removal, resuspended in 2% low melting point agarose. The agarose mitochondria pellets were then embedded for electron microscopy using 2% OsO₄ for 4 h followed by ethanol/acetone dehydration and Epon embedding (Serva). To analyze mitochondrial morphology in cerebellar cells in situ, we perfused 2- to 3-month-old animals with 5 ml of Hank's Balanced Salt Solution with heparin (19.5 U ml⁻¹), followed by 30 ml of fixative as described. The brain was extracted and further postfixed for 8 h at 4 °C in fixative. Cerebella were dissected and sectioned in thin slices, < 1 mm. Sections were further dissected in pieces of two to three lobes and postfixed with 2% OsO₄ and 1.5% ferrocyanide (Science Services), dehydrated by ethanol/acetone, and Epon embedded. Epon blocks were further trimmed, and 50 nm thick sections (Leica UltraCut2) were obtained from the thickest part of the sample. The sections were post-stained with 4% uranylacetate for 30 min followed by lead citrate for 5 min.

For isolated mitochondria, the imaging area was performed 20–50 μ m away from the pellet edge with a JEM-1400 Transmission Electron Microscope (Jeol Tokyo) using $\times 20,000$ original magnification. Quantification for the mitochondria morphology in cerebellum tissue was done at $\times 6,000$ – $\times 20,000$ original magnification.

For data analysis, the investigator was blinded for the genetic background of samples. The open source software ImageJ/Fiji⁷¹ was used to define total

mitochondrial perimeter and percent mitochondrial perimeter in ≤ 30 nm of distance to the ER. In the case of GC, a larger number of cells had to be analyzed because of cellular morphology. GC somata are densely packed in the GCL, with a small region of cytoplasm around the nucleus giving space to only one to four mitochondria per 50 nm section. Therefore, statistical analysis was performed on mitochondria as a unit (Fig. 7b).

Statistics. Datasets with groups of $n < 12$ are represented as dot plots with underlying bar graph with mean \pm s.e.m. (standard error of the mean). Datasets with groups of $n \geq 12$ are represented as box plots consisting of median, box spanning quartiles 1–3 (Q1–Q3) and whiskers to the maximum and minimum value. Data distribution was tested for normality using the Shapiro–Wilk normality test to determine statistical tests, and individual data points are shown in graphs. Exclusion of data points was performed only in oxygen consumption measurements for technical replicates in which one of the multiple injections failed during the experiment; no other data points were excluded. The statistical details for each experiment can be found in the figure legend, and further information (sample size, n of independent experiments, testing and P values) is provided in Supplementary Table 4. A P value < 0.05 was considered statistically significant and indicated by asterisks (* $P < 0.05$; ** $P < 0.01$; *** $P < 0.001$). Statistical analyses were performed using Microsoft Excel 2016 and GraphPad Prism (v.7/8; GraphPad Software). No statistical methods were used to predetermine sample sizes, but the chosen sample sizes are similar to those reported in previous publications (for example, Brill et al.⁶⁹, Baughman et al.²⁷ and Pagliarini et al.⁷). Samples were not randomized during data collection, and mice were assigned to experimental groups according to genotype. Randomization was not possible due to constraints in animal availability and determination of experiment by given genotypes. Data collection and analysis were performed blind to the conditions in the following experiments: Figs. 1g, 7b and 7e. In all other experiments, the experimenters were not blinded. Further information on research design is available in the Nature Research Reporting Summary linked to this article and in Supplementary Table 4.

Accession codes. The mass spectrometry proteomics data have been deposited to the ProteomeXchange Consortium via the PRIDE partner repository with the dataset identifier: mitochondria from PC (PXD010772), from GC (PXD010774) and from astrocytes (PXD010781); and whole cerebellum (PXD013380).

Reporting Summary. Further information on the research design is available in the Nature Research Reporting Summary linked to this article.

Data availability

All proteomics data generated within this study are deposited to the ProteomeXchange Consortium via the PRIDE44 partner repository with the dataset identifiers PXD010772, PXD010774, PXD010781 and PXD013380. In addition, Supplementary Data provide information on the proteomics data analysis used for the conclusions in the main and supplementary figures. All additional data that support the findings of this study are available from the corresponding author upon reasonable request. The *MitoTag* mouse line is available from The Jackson Laboratory as JAX#032675 (Rosa26-CAG-LSL-GFP-OMM). The Mcu^{FL/FL} and the Rbp4:Cre mouse strains are protected under a material transfer agreement with the MMRR (C57BL/6N-Mcutm1a(EUCOMM)Hmgu/H; Tg(Rbp4-cre)KL100Gsat/Mmucd), and the Rmdn3^{-/-} mouse strain is protected under a material transfer agreement with the KOMP Repository (KO mouse project 3U01HG004080).

References

- Yoshii, S. R., Kishi, C., Ishihara, N. & Mizushima, N. Parkin mediates proteasome-dependent protein degradation and rupture of the outer mitochondrial membrane. *J. Biol. Chem.* **286**, 19630–19640 (2011).
- Horie, C., Suzuki, H., Sakaguchi, M. & Mihara, K. Characterization of signal that directs C-tail-anchored proteins to mammalian mitochondrial outer membrane. *Mol. Biol. Cell* **13**, 1615–1625 (2002).
- Hitz, C., Steuber-Buchberger, P., Delic, S., Wurst, W. & Kühn, R. Generation of shRNA transgenic mice. *Methods Mol. Biol.* **530**, 101–129 (2009).
- Ortiz, O., Wurst, W. & Kühn, R. Reversible and tissue-specific activation of MAP kinase signaling by tamoxifen in Braff(V637)ER(T2) mice. *Genesis* **51**, 448–455 (2013).
- Hitz, C., Wurst, W. & Kühn, R. Conditional brain-specific knockdown of MAPK using Cre/loxP regulated RNA interference. *Nucl. Acids Res.* **35**, e90 (2007).
- Breckwoldt, M. O. et al. Multiparametric optical analysis of mitochondrial redox signals during neuronal physiology and pathology in vivo. *Nat. Med.* **20**, 555–560 (2014).
- Gorski, J. A. et al. Cortical excitatory neurons and glia, but not GABAergic neurons, are produced in the Emx1-expressing lineage. *J. Neurosci.* **22**, 6309–6314 (2002).
- Rossi, J. et al. Melanocortin-4 receptors expressed by cholinergic neurons regulate energy balance and glucose homeostasis. *Cell Metab.* **13**, 195–204 (2011).

60. Barski, J. J., Dethleffsen, K. & Meyer, M. Cre recombinase expression in cerebellar purkinje cells. *Genesis* **28**, 93–98 (2000).
61. Fünfschilling, U. & Reichardt, L. F. Cre-mediated recombination in rhombic lip derivatives. *Genesis* **33**, 160–169 (2002).
62. Gregorian, C. et al. Pten deletion in adult neural stem/progenitor cells enhances constitutive neurogenesis. *J. Neurosci.* **29**, 1874–1886 (2009).
63. Gong, S. et al. Targeting Cre recombinase to specific neuron populations with bacterial artificial chromosome constructs. *J. Neurosci.* **27**, 9817–9823 (2007).
64. Gong, S. et al. A gene expression atlas of the central nervous system based on bacterial artificial chromosomes. *Nature* **425**, 917–925 (2003).
65. Busche, M. A. et al. Clusters of hyperactive neurons near amyloid plaques in a mouse model of alzheimer's disease. *Science* **321**, 1686–1689 (2008).
66. Gurney, M. E. et al. Motor neuron degeneration in mice that express a human Cu,Zn superoxide dismutase mutation. *Science* **264**, 1772–1775 (1994).
67. Rodriguez, C. I. et al. High-efficiency deleter mice show that FLPe is an alternative to Cre-loxP. *Nat. Genet.* **25**, 139–140 (2000).
68. Skarnes, W. C. et al. A conditional knockout resource for the genome-wide study of mouse gene function. *Nature* **474**, 337–342 (2011).
69. Brill, M. S. et al. Branch-specific microtubule destabilization mediates axon branch loss during neuromuscular synapse elimination. *Neuron* **92**, 845–856 (2016).
70. Kleele, T. et al. An assay to image neuronal microtubule dynamics in mice. *Nat. Commun.* **5**, 4827 (2014).
71. Schindelin, J. et al. Fiji: an open-source platform for biological-image analysis. *Nat. Methods* **9**, 676–682 (2012).
72. Wettmarshausen, J. & Perocchi, F. Isolation of functional mitochondria from cultured cells and mouse tissues. *Methods Mol. Biol.* **1567**, 15–32 (2017).
73. Franko, A. et al. Efficient isolation of pure and functional mitochondria from mouse tissues using automated tissue disruption and enrichment with anti-TOM22 magnetic beads. *PLoS One* **8**, e82392 (2013).
74. Sims, N. R. & Anderson, M. F. Isolation of mitochondria from rat brain using percoll density gradient centrifugation. *Nat. Protoc.* **3**, 1228–1239 (2008).
75. Wang, X. et al. Isolation of brain mitochondria from neonatal mice. *J. Neurochem.* **119**, 1253–1261 (2011).
76. Watkins, P. A., Ferrell, E. V. Jr., Pedersen, J. I. & Hoefler, G. Peroxisomal fatty acid beta-oxidation in HepG2 cells. *Arch. Biochem. Biophys.* **289**, 329–336 (1991).
77. Demarquoy, J. & Le Borgne, F. Crosstalk between mitochondria and peroxisomes. *World J. Biol. Chem.* **6**, 301–309 (2015).
78. Wiśniewski, J. R., Zougman, A., Nagaraj, N. & Mann, M. Universal sample preparation method for proteome analysis. *Nat. Methods* **6**, 359–362 (2009).
79. Rappsilber, J., Ishihama, Y. & Mann, M. Stop and go extraction tips for matrix-assisted laser desorption/ionization, nanoelectrospray, and LC/MS sample pretreatment in proteomics. *Anal. Chem.* **75**, 663–670 (2003).
80. Cox, J. et al. Accurate proteome-wide label-free quantification by delayed normalization and maximal peptide ratio extraction, termed MaxLFQ. *Mol. Cell Proteom.* **13**, 2513–2526 (2014).
81. Vizcaino, J. A. et al. update of the PRIDE database and its related tools. *Nucl. Acids Res.* **44**, D447–456 (2016).
82. Tyanova, S. et al. The Perseus computational platform for comprehensive analysis of (prote)omics data. *Nat. Methods* **13**, 731–740 (2016).
83. Cox, J. & Mann, M. 1D and 2D annotation enrichment: a statistical method integrating quantitative proteomics with complementary high-throughput data. *BMC Bioinform.* **13** (Suppl. 16), S12 (2012).
84. Goldberg, T. et al. LocTree3 prediction of localization. *Nucl. Acids Res.* **42**, W350–W355 (2014).
85. Wang, J., Vasaiakar, S., Shi, Z., Greer, M. & Zhang, B. WebGestalt 2017: a more comprehensive, powerful, flexible and interactive gene set enrichment analysis toolkit. *Nucl. Acids Res.* **45**, W130–W137 (2017).
86. Kanehisa, M., Goto, S., Sato, Y., Furumichi, M. & Tanabe, M. KEGG for integration and interpretation of large-scale molecular data sets. *Nucl. Acids Res.* **40**, D109–D114 (2011).
87. Shin, J. B. et al. Molecular architecture of the chick vestibular hair bundle. *Nat. Neurosci.* **16**, 365–374 (2013).
88. Uchida, Y. & Takahashi, H. Rapid detection of Abeta deposits in APP transgenic mice by Hoechst 33342. *Neurosci. Lett.* **448**, 279–281 (2008).
89. Tillberg, P. W. et al. Protein-retention expansion microscopy of cells and tissues labeled using standard fluorescent proteins and antibodies. *Nat. Biotechnol.* **34**, 987–992 (2016).

Reporting Summary

Nature Research wishes to improve the reproducibility of the work that we publish. This form provides structure for consistency and transparency in reporting. For further information on Nature Research policies, see [Authors & Referees](#) and the [Editorial Policy Checklist](#).

Statistics

For all statistical analyses, confirm that the following items are present in the figure legend, table legend, main text, or Methods section.

n/a Confirmed

- The exact sample size (n) for each experimental group/condition, given as a discrete number and unit of measurement
- A statement on whether measurements were taken from distinct samples or whether the same sample was measured repeatedly
- The statistical test(s) used AND whether they are one- or two-sided
Only common tests should be described solely by name; describe more complex techniques in the Methods section.
- A description of all covariates tested
- A description of any assumptions or corrections, such as tests of normality and adjustment for multiple comparisons
- A full description of the statistical parameters including central tendency (e.g. means) or other basic estimates (e.g. regression coefficient) AND variation (e.g. standard deviation) or associated estimates of uncertainty (e.g. confidence intervals)
- For null hypothesis testing, the test statistic (e.g. F , t , r) with confidence intervals, effect sizes, degrees of freedom and P value noted
Give P values as exact values whenever suitable.
- For Bayesian analysis, information on the choice of priors and Markov chain Monte Carlo settings
- For hierarchical and complex designs, identification of the appropriate level for tests and full reporting of outcomes
- Estimates of effect sizes (e.g. Cohen's d , Pearson's r), indicating how they were calculated

Our web collection on [statistics for biologists](#) contains articles on many of the points above.

Software and code

Policy information about [availability of computer code](#)

Data collection

Open source software: μ Manager 1.48v (MM core version 8.4.0; MM studio version 1.4.22) for acquisition of mitochondrial transport; Seahorse XFe96 Wave, Seahorse Bioscience, Inc., (version 2.3.0.19.) for oxygen consumption measurements.
Commercial software: for Q-Exactive Tune (2.8 SP1 build 2806) & XCalibur (version 3.1.66.10), Thermo Fisher Scientific for mass spectrometry; for Q-Exactive HF Tune 2.8 (SP1 build 2806) & XCalibur (version 4.0.27.19), Thermo Fisher Scientific for mass spectrometry; Summit software, Dako for flow cytometry; FUSION-CAPT Advance FX7, Vilber Lourmat (version 16.12) for Western blot development; FV10-ASW, Olympus (version 4.2) for confocal microscopy; FV31S-SW, Olympus for confocal microscopy; TEM Center, Jeol Tokyo for electron microscopy; CLARIOstar (software version 5.20 R5) for calcium uptake assay.

Data analysis

Open source software: ImageJ/Fiji (version 1.51u) for processing of images; Seahorse XFe96 Wave, Seahorse Bioscience, Inc., (version 2.3.0.19.) for processing of oxygen consumption measurements; GraphPad (version 7) for statistics and figure representation; Microsoft Excel 2016 (version 16.0.6741.2048) for statistics; Image Studio Lite, Licor (version 5.2.5) for Western blot analysis; MaxQuant (version 1.5.1.1; version 1.5.5.1) for processing of mass spectrometry; Perseus (version 1.6.1.1.) for analysis of proteomic data and statistics.
Open source online tools: WebGestalt 2017 (update 1/27/2017) for analysis of proteomic data; Kegg mapper (version v3.1 released October 1, 2017) for analysis of proteomic data; Venn diagram (<http://bioinformatics.psb.ugent.be/webtools/Venn/>) for figure representation.
Commercial software: FlowJo software (version 10.5), TreeStar (version 10) for analysis of flow cytometry data; Adobe Photoshop CS5, (version 12.0) for image processing; Adobe Illustrator CS5, (version 15.0.0) for figure representation.

For manuscripts utilizing custom algorithms or software that are central to the research but not yet described in published literature, software must be made available to editors/reviewers. We strongly encourage code deposition in a community repository (e.g. GitHub). See the Nature Research [guidelines for submitting code & software](#) for further information.

Data

Policy information about [availability of data](#)

All manuscripts must include a [data availability statement](#). This statement should provide the following information, where applicable:

- Accession codes, unique identifiers, or web links for publicly available datasets
- A list of figures that have associated raw data
- A description of any restrictions on data availability

All proteomic data generated within this study are deposited to the ProteomeXchange Consortium via the PRIDE44 partner repository with the dataset identifiers: PXD010772, PXD010774, PXD010781 and PXD013380. Additionally, Supplementary Data Table 1 provides information on the proteomics data analysis used for the conclusions in the main and supplementary figures.

The MitoTag mouse line will be available from The Jackson Laboratory as JAX#032675 (Rosa26-CAG-LSL-GFP-OMM). The McuFL/FL and the Rbp4:Cre mouse strain are protected under a material transfer agreement with the MMRRC (C57BL/6N-Mcutm1a(EUCOMM)HmgU/H; Tg(Rbp4-cre)KL100Gsat/Mmucd), and the Rmdn3 -/- mouse strain is protected under a material transfer agreement with the KOMP Repository (KO mouse project 3U01HG004080).

Field-specific reporting

Please select the one below that is the best fit for your research. If you are not sure, read the appropriate sections before making your selection.

- Life sciences Behavioural & social sciences Ecological, evolutionary & environmental sciences

For a reference copy of the document with all sections, see [nature.com/documents/nr-reporting-summary-flat.pdf](https://www.nature.com/documents/nr-reporting-summary-flat.pdf)

Life sciences study design

All studies must disclose on these points even when the disclosure is negative.

Sample size	No statistical methods were used to pre-determine sample sizes but the chosen sample sizes are similar to those reported in previous publications (e.g. Brill et al. Neuron 2016; Baughman et al., Nature 2011 ; Pagliarini et al. Cell, 2008).
Data exclusions	Exclusion of data points was only performed in oxygen consumption measurements for technical replicates in which one of the multiple injections failed during the experiment; no other data points were excluded.
Replication	All attempts to replicate were successful. To ensure reproducibility experiments were independently repeat at least three times with the following exceptions: Figure 7b: data is representative for two biological replicates with N=160/133/120 mitochondria from N=10/72/16 individual cells. Supplementary Figure 3d: data is representative for four biological replicates with N=88/83 NMJ areas and N=56/54 AChR density measurements.
Randomization	Samples were not randomized during data collection and animals assigned to experimental groups according to genotype. Randomization was not possible due to constraints in animal availability, and determination of experiment by given genotype.
Blinding	Blinding was applied to the following experiments: Supplementary Figure 3a: Mitochondrial transport measurements were analyzed by blinded investigator. Figure 1g & Supplementary Figure 3e: Isolation were performed by C.F. with information on genotype. Further oxygen consumption measurements and analysis were performed by L.T. in a blinded way. Figure 7b and 7e: Data were acquired by a blinded investigator with no information on genotypes. For analysis, it was not possible to blind the investigator for the different cell types (PC, GC, A) due to unique structural features.

Reporting for specific materials, systems and methods

We require information from authors about some types of materials, experimental systems and methods used in many studies. Here, indicate whether each material, system or method listed is relevant to your study. If you are not sure if a list item applies to your research, read the appropriate section before selecting a response.

Materials & experimental systems

- | n/a | Involved in the study |
|-------------------------------------|---|
| <input type="checkbox"/> | <input checked="" type="checkbox"/> Antibodies |
| <input checked="" type="checkbox"/> | <input type="checkbox"/> Eukaryotic cell lines |
| <input checked="" type="checkbox"/> | <input type="checkbox"/> Palaeontology |
| <input type="checkbox"/> | <input checked="" type="checkbox"/> Animals and other organisms |
| <input type="checkbox"/> | <input checked="" type="checkbox"/> Human research participants |
| <input checked="" type="checkbox"/> | <input type="checkbox"/> Clinical data |

Methods

- | n/a | Involved in the study |
|-------------------------------------|--|
| <input checked="" type="checkbox"/> | <input type="checkbox"/> ChIP-seq |
| <input type="checkbox"/> | <input checked="" type="checkbox"/> Flow cytometry |
| <input checked="" type="checkbox"/> | <input type="checkbox"/> MRI-based neuroimaging |

Antibodies used

Name : Supplier , Catalog # , clone (lot) ; Dilution:

Acads : Abcam , ab156571 , EPR10862(B) (lot: GR117677-4) ; Dilution: IF - 1: 200 ;
 Ak3 : Santa Cruz , sc-398571 , E-5 (lot: E1616) ; Dilution: IF - 1: 100 ;
 Ak4 : Santa Cruz , sc-271161 , A-9 (lot: A0512) ; Dilution: WB - 1: 100 ; IF - 1: 100 ;
 Amyloid- β (1-16)-AF647 : BioLegend , 803020 , 6E10 (lot: B250539) ; Dilution: IF - 1: 500 ;
 Amyloid- β (17-24) : BioLegend , 800712 , 4G8 (lot: NaN) ; Dilution: IF - 1: 1000 ;
 Amyloid- β (8-17) : Dako , M0872 , 6F/3D (lot: 00086092) ; Dilution: IF - 1: 100 ;
 Anti-chicken IgY-Alexa Fluor 488 : ThermoScientific , A-11039 , - (lot: 1599396 , 1899514) ; Dilution: IF - 1: 1000 ;
 Anti-chicken IgY-Alexa Fluor 647 : ThermoScientific , A-21449 , - (lot: 1622573) ; Dilution: IF - 1: 1000 ;
 Anti-mouse IgG1-Alexa Fluor 594 : ThermoScientific , A-21125 , - (lot: 41652A) ; Dilution: IF - 1: 1000 ;
 Anti-mouse IgG-Alexa Fluor 647 : Jackson ImmunoResearch , 715-605-151 , - (lot: 127051) ; Dilution: IF - 1: 2000 ;
 Anti-mouse IgG-HRP : BioRad , 1706516 , - (lot: NaN) ; Dilution: WB - 1: 5000 ;
 Anti-rabbit IgG-Alexa Fluor 555 : ThermoScientific , A-31572 , - (lot: 1806147) ; Dilution: IF - 1: 2000 ;
 Anti-rabbit IgG-Alexa Fluor 568 : ThermoScientific , A-11011 , - (lot: NaN) ; Dilution: IF - 1: 1000 ;
 Anti-rabbit IgG-Alexa Fluor 594 : ThermoScientific , A-11012 , - (lot: 1310680) ; Dilution: IF - 1: 1000 ;
 Anti-rabbit IgG-HRP : BioRad , 1706515 , - (lot: 64170140) ; Dilution: WB - 1: 5000 ;
 ATP5a : Abcam , ab14748 , 15H4C4 (lot: GR303070-4) ; Dilution: WB - 1: 10000 ;
 Beta-Actin : Sigma , A2228 , AC-74 (lot: 058M4808V) ; Dilution: WB - 1: 4000 ;
 Calreticulin : CellSignaling , #12238 , D3E6 (lot: 0004) ; Dilution: WB - 1: 1000 ;
 Catalase : Rockland , 100-4151 , - (lot: 18043) ; Dilution: IF - 1: 200 ;
 ChAT : Sigma , AB144P , - (lot: 3167107) ; Dilution: IF - 1: 500 ;
 Cox4i1 : Abgent , AP22111a , RB55992 (lot: SA160128HA) ; Dilution: WB - 1: 1000 ; IF - 1: 200 ;
 Cpt1a : ProteinTech , 15184-1-AP , - (lot: 00052905) ; Dilution: IF - 1: 50 ;
 CypD : Abcam , ab110324 , E11AE12BD4 (lot: GR316345-2) ; Dilution: WB - 1: 5000 ;
 Emre (C22orf32) : Santa Cruz , sc-86337 , C-12 (lot: K0415) ; Dilution: WB - 1: 500 ;
 Gfap : Abcam , ab4674 , - (lot: GR1473-13) ; Dilution: IF - 1: 2000 ;
 GFP : Abcam , ab13970 , - (lot: GR236651-23) ; Dilution: IF - 1: 1000 ;
 GFP : Santa Cruz , sc-9996 , B-2 (lot: K1815) ; Dilution: WB - 1: 500 ;
 Gldc : Sigma , HPA002318 , - (lot: C106148) ; Dilution: WB - 1: 1000 ; IF - 1: 400 ;
 Glis (KGA) : ProteinTech , 20170-1-AP , - (lot: 00012602) ; Dilution: IF - 1: 200 ;
 Glis2 (C-term E513) : Abgent , AP6650d , RB20072 (lot: SA101018BU) ; Dilution: IF - 1: 400 ;
 Got2 : Abcam , ab171739 , EPR12354(B) (lot: GR170733-1) ; Dilution: WB - 1: 1000 ; IF - 1: 400 (human: 1:2000) ;
 ImmPRESS[®] HRP Anti-Rabbit IgG (Peroxidase) Polymer Detection Kit : Vector Lab , MP-7451 , - (lot: ZD0602) ; Dilution: IF - ready-to-use ;
 Lamin B1 : Abcam , ab16048 , - (lot: 429044) ; Dilution: WB - 1: 1000 ;
 Ldhd : Abcam , ab182146 , EPR15068(B) (lot: GR152139-1) ; Dilution: IF - 1: 100 ;
 MaoB : Santa Cruz , sc-515354 , D-6 (lot: C0816) ; Dilution: IF - 1: 100 ;
 Mavs : CellSignaling , #4983 , - (lot: 0003) ; Dilution: IF - 1: 200 ;
 Mcu : Sigma , HPA016480 , - (lot: CD114474) ; Dilution: WB - 1: 1000 ; IF - 1: 400 (human: 1:200) ;
 Mouse IgG1-APC : Miltenyi Biotec , 130-113-758 , IS5-21F5 (lot: NaN) ; Dilution: WB - 1: 25 ;
 NeuN : Sigma , MAB377 , A60 (lot: 2742283) ; Dilution: IF - 1: 100 ;
 NeuN-488 : Abcam , ab190195 , EPR12763 (lot: GR3233763-2) ; Dilution: IF - 1: 50 ;
 Nipsnap1 : CellSignaling , #13226 , D1Y6S (lot: 0001) ; Dilution: IF - 1: 200 ;
 Ociad2 : Sigma , HPA040979 , - (lot: C91827) ; Dilution: WB - 1: 1000 ; IF - 1: 200 (human: 1:500) ;
 Ociad2 : Abcam , ab91576 , (lot: GR265190-2) ; Dilution: IF - 1: 200 ;
 Pex14 : Denis Crane ; (lot: NaN) ; Dilution: IF - 1: 1000 ;
 Pptc7 : Abcam , ab122548 , - (lot: GR134884-4) ; Dilution: IF - 1: 200 ;
 Rabbit IgG zenon AlexaFluor 647 Kit : ThermoScientific , Z25308 , - (lot: 2021736) ; Dilution: IF - 10 microl/1 microg antibody ;
 Rmdn3 (Fam82a2) : Abcam , ab189845 , - (lot: GR26796-1) ; Dilution: WB - 1: 2000 ; IF - 1: 400 (human: 1:2000) ;
 Sfxn5 : Abcam , ab172971 , EPR9532 (lot: YK020618C5) ; Dilution: WB - 1: 2000 ; IF - 1: 500 ;
 SNAP25 : CellSignaling , #5308 , D7B4 (lot: 0001) ; Dilution: WB - 1: 2000 ; ;
 Snph : Abcam , ab192605 , EPR14115(2) (lot: GR300418-5) ; Dilution: IF - 1: 200 ;
 Tom22-APC : Miltenyi Biotec , 130-107-733 , 1C9-2 (lot: NaN) ; Dilution: WB - 1: 25 ;
 Tomm20 : Abcam , ab78547 , - (lot: GR3199811-3) ; Dilution: WB - 1: 1000 ;
 tRFP : Evrogen , AB234 , - (lot: 23301301013) ; Dilution: WB - 1: 5000 ;
 Tst : Abcam , ab166625 , EPR11646(B) (lot: YJ1120015) ; Dilution: IF - 1: 500 (human: 1:2000) .

Validation

Name (Supplier , Catalog #) : Validation ;

Acads (Abcam , ab156571) : Data sheet: mouse, IF; Ref: doi: 10.1111/jcmm.12828 ;
 Ak3 (Santa Cruz , sc-398571) : Data sheet: mouse, IF ;
 Ak4 (Santa Cruz , sc-271161) : Data sheet: mouse, IF ;
 Amyloid- β (1-16)-AF647 (BioLegend , 803020) : Data sheet: human, Tg-mouse, IF; Ref:doi: 10.1073/pnas.0813404106; PMID: 10028915 ;
 Amyloid- β (17-24) (BioLegend , 800712) : Data sheet: human, Tg-mouse, IF; Ref: PMID: 10028915 ;
 Amyloid- β (8-17) (Dako , M0872) : Data sheet: human, IHC; Ref: PMID: 10028915 ;
 Anti-chicken IgY-Alexa Fluor 488 (ThermoScientific , A-11039) : RRID:AB_2534096; 168 citations ;
 Anti-chicken IgY-Alexa Fluor 647 (ThermoScientific , A-21449) : RRID:AB_2535866; 40 citations ;
 Anti-mouse IgG1-Alexa Fluor 594 (ThermoScientific , A-21125) : RRID:AB_2535767; 22 citations ;
 Anti-mouse IgG-Alexa Fluor 647 (Jackson ImmunoResearch , 715-605-151) : RRID:AB_2340863; 26 citations ;

Anti-mouse IgG-HRP (BioRad , 1706516): RRID: AB_11125547; Ref: doi: 10.1016/j.cell.2016.07.041; WB, rat ;
 Anti-rabbit IgG-Alexa Fluor 555 (ThermoScientific , A-31572): RRID:AB_162543; 115 citations ;
 Anti-rabbit IgG-Alexa Fluor 568 (ThermoScientific , A-11011): RRID:AB_143157; 251 citations ;
 Anti-rabbit IgG-Alexa Fluor 594 (ThermoScientific , A-11012): RRID:AB_2534079; 215 citations ;
 Anti-rabbit IgG-HRP (BioRad , 1706515): RRID:AB_2617112; Ref: doi: 10.1016/j.cell.2016.07.041; WB, rat ;
 ATP5a (Abcam , ab14748): Data sheet: mouse, WB; Ref: doi: 10.1111/accel.12715 ;
 Beta-Actin (Sigma , A2228): Data sheet: mouse, WB ;
 Calreticulin (CellSignaling , #12238): Data sheet: mouse, WB ;
 Catalase (Rockland , 100-4151): Data sheet: mouse, IF ;
 ChAT (Sigma , AB144P): Data sheet: mouse, WB ;
 Cox4i1 (Abgent , AP22111a): Data sheet: mouse, IF ;
 Cpt1a (ProteinTech , 15184-1-AP): Data sheet: mouse, IF; Ref:doi: 10.1038/emm.2017.243 ;
 CypD (Abcam , ab110324): Data sheet: mouse, WB; KO validation: Ref: doi: 10.1016/j.expneurol.2009.02.015 ;
 Emre (C22orf32) (Santa Cruz , sc-86337): Data sheet: mouse, WB; Ref: doi: 10.1016/j.celrep.2017.02.032 ;
 Gfap (Abcam , ab4674): Data sheet: mouse, human, IF; Ref: doi: 10.1177/1759091415601636 ;
 GFP (Abcam , ab13970): Data sheet: mouse, IF ;
 GFP (Santa Cruz , sc-9996): Data sheet: mouse, WB ;
 Gldc (Sigma , HPA002318): Data sheet: mouse, IF; siRNA KD validation ;
 Gls (KGA) (ProteinTech , 20170-1-AP): Data sheet: mouse, IF; Ref:doi: 10.1038/s41598-017-16327-z ;
 Gls2 (Abgent , AP6650d): Data sheet: mouse, IF ;
 Got2 (Abcam , ab171739): Data sheet: mouse, IF; Ref:doi: 10.1186/s13024-017-0219-3. ;
 ImmPRESS® HRP Anti-Rabbit IgG (Peroxidase) Polymer Detection Kit (Vector Lab , MP-7451): RRID:AB_2336529; 7 citations;
 Ref: doi: 10.1172/JCI92300.; mouse, IF ;
 Lamin B1 (Abcam , ab16048): Data sheet: mouse, WB; KO validation in cells ;
 Ldhd (Abcam , ab182146): Data sheet: mouse, human, WB. ;
 MaoB (Santa Cruz , sc-515354): Data sheet: mouse, IF ;
 Mavs (CellSignaling , #4983): Data sheet: mouse, IF ;
 Mcu (Sigma , HPA016480): Data sheet: mouse, IF; KO validation: This study ;
 Mouse IgG1-APC (Miltenyi Biotec , 130-113-758): RRID:AB_2733439; Ref: doi: 10.1016/j.ab.2009.02.040; isolation, FACS,
 mouse ;
 NeuN (Sigma , MAB377): Data sheet: human, IF ;
 NeuN-488 (Abcam , ab190195): Data sheet: human, IF; Ref: doi: 10.1152/ajpgi.00371.2016 ;
 Nipsnap1 (CellSignaling , #13226): Data sheet: human, mouse, WB ;
 Ociad2 (Sigma , HPA040979): Data sheet: human, IF; human, WB ;
 Ociad2 (Abcam , ab91576): Data sheet: mouse, human, WB ;
 Pex14 (Denis Crane , -): Ref: doi: 10.1242/jcs.02776: mouse, WB, IF ;
 Pptc7 (Abcam , ab122548): Data sheet: mouse, IF ;
 Rabbit IgG zenon AlexaFluor 647 Kit (ThermoScientific , Z25308): RRID:AB_2736962; Ref: doi: 10.1128/JVI.01457-17; mouse, IF ;
 Rmdn3 (Fam82a2) (Abcam , ab189845): Data sheet: mouse, IF; KO validation: This study ;
 Sfxn5 (Abcam , ab172971): Data sheet: mouse, human, WB ;
 SNAP25 (CellSignaling , #5308): Data sheet: mouse, WB ;
 Snph (Abcam , ab192605): Data sheet: mouse, IF ;
 Tom22-APC (Miltenyi Biotec , 130-107-733): RRID:AB_2654220; Ref: doi: 10.1016/j.ab.2009.02.040; isolation, FACS, mouse ;
 Tomm20 (Abcam , ab78547): Data sheet: human, WB, IF ;
 tRFP (Evrogen , AB234): Data sheet: mouse, WB ;
 Tst (Abcam , ab166625): Data sheet: mouse, IF .

Animals and other organisms

Policy information about [studies involving animals](#); [ARRIVE guidelines](#) recommended for reporting animal research

Laboratory animals	Male and female animals of the species <i>Mus musculus</i> /C57BL/6 (mixed N/J) background were used between 6 weeks to 6 month.
Wild animals	Study did not involve wild animals.
Field-collected samples	Study did not involve field-collected samples.
Ethics oversight	All animal experiments were approved by the responsible regulatory agencies (Regierung von Oberbayern).

Note that full information on the approval of the study protocol must also be provided in the manuscript.

Human research participants

Policy information about [studies involving human research participants](#)

Population characteristics	Male and female patients, 52-91 years of age; three groups: no relevant diagnosis; Alzheimer's disease, ALS
Recruitment	Tissue selected from archival autopsy material.
Ethics oversight	Use of human samples was in accordance with institutional ethical guidelines and approved by the ethics committee of the University of Geneva (Switzerland).

Flow Cytometry

Plots

Confirm that:

- The axis labels state the marker and fluorochrome used (e.g. CD4-FITC).
- The axis scales are clearly visible. Include numbers along axes only for bottom left plot of group (a 'group' is an analysis of identical markers).
- All plots are contour plots with outliers or pseudocolor plots.
- A numerical value for number of cells or percentage (with statistics) is provided.

Methodology

Sample preparation

The crude mitochondrial fraction (CMF) from 20 mg mouse cortex samples was resuspended in 100 μ l 4% PFA/PBS and incubated in the dark for 5 minutes at room temperature. Samples were washed three times with PBS and resuspended in 100 μ l. 20 μ l fixed mitochondria were used per staining. First the sample was washed once with 0.5% BSA/PBS and then incubated with APC-conjugated antibodies: IgG1 or Tom22 (Miltenyi Biotec, 1:25) in the dark, 4°C, 60 rpm for 60 minutes. Samples were washed three times with 0.5%BSA/PBS and finally resuspended in 100 μ l PBS.

Instrument

Samples were acquired on a CyAn ADP 9 flow cytometer (Beckman Coulter) with the following laser lines: 405, 488, 642 nm.

Software

Data was acquired with the Summit software (Dako) and further analyzed with FlowJo, TreeStar (version 10).

Cell population abundance

No sorting was performed.

Gating strategy

To allow for optimal identification and separation of small particles, the flow rate was adjusted accordingly and optical parameters were scaled logarithmically. The gate was adjusted to exclude a PBS+BSA probe (buffer only; negative) in each experiment. Mitochondria were gated by FSC and SSC, as well as pulse width to discriminate doublets. Then Tom22-APC staining (APC, 665/20) intensities were gated against IgG1-APC control samples to define mitochondria (on average 34.27 \pm 1.62%). From this, individual gates for GFP-OMM (FITC, 530/40) and mito-RFP (PE, 575/25) were adjusted according to wild type mitochondria (Tom22+).

- Tick this box to confirm that a figure exemplifying the gating strategy is provided in the Supplementary Information.